doi：10. 11823/j. issn. 1674 －5795. 2018. 03. 01

# Stroboscopic White Light Interferometry（SWLI）

Liang-Chia Chen
（National Taiwan University，Taipei 10617，China）

**Abstract**：Stroboscopic white light interferometry（SWLI）has been known as a useful measurement technique for vibrating samples such asmicro electro mechanical systems（MEMS）or micro-opto-electro-mechanical systems（MOEMS）because it enables dynamic mode reconstruction and characterization of the tested system. The technique has been extended to measure a microstructure having an individual vibrating excitation source which cannot be detected or analyzed in advance by the traditional stroboscopic method. To provide a comprehensive insight into this newly developed technique，this chapter presents the theory，technical methodology and experimental results as well as analyses of the techniques for various applications. The technology provides an effective method in reconstructing and analyzing dynamic behavior of MEMS，MOEMS or even bio-objects in a micro-or nano-scale. Some experimental results and analyses have been provided to verify the feasibility and accuracy of the developed techniques with respect to various applications.

**Key words**：white light interferometry；dynamic measurement；stroboscopic white light interferometry（SWLI）；micro electro mechanical systems（MEMS）；micro-opto-electro-mechanical systems（MOEMS）

**中图分类号**：TB92　　**文献标识码**：A　　**文章编号**：1674 －5795（2018）03 －0001 －30

# 频闪白光干涉技术

陈亮嘉
（台湾大学，台湾 台北 10617）

**摘　要**：频闪白光干涉技术（SWLI）能够对被测系统进行动态模式的重建和表征，在微机电系统（MEMS）或微光机电系统（MOEMS）等振动样品测量中具有很高的实用性。传统频闪方法不能预先检测或分析具有单个振动激励源的微结构，而频闪白光干涉技术则解决了这一问题。为全面了解这一新开发的技术，本文从理论、技术方法和该技术各种应用的实验结果及分析进行了介绍。该技术为 MEMS，MOEMS 甚至微纳尺度生物体动态性能的重建和分析提供了一种有效的方法。实验结果和分析证明了频闪白光干涉技术在实际应用中具有良好的可行性和准确性。

**关键词**：白光干涉法；动态测量；频闪白光干涉法（SWLI）；微机电系统（MEMS）；微光机电系统（MOEMS）

## 0　Introduction

In the last two decades，white light interferometry（WLI）has been well established as an accurate measurement technique with a long measurement range，thus enabling it to develop a wide application area for characterizing microsystems or micro structures. WLI is mainly used for measuring the characteristic of static surfaces. In additional to static profile measurements，one of the important applications of WLI is dynamic characterization of vibrating samples，such as micro electro mechanical systems（MEMS）or micro-opto-electro-mechanical systems（MOEMS）[1]. Combining stroboscopic lighting and WLI can freeze the motion of vibrating samples at the instant when interferogram images are acquired. Therefore，measuring vibrating samples is similar to measuring static ones. The stroboscopic interferometer was introduced in 1979 for the measurement of objects in the presence of severe acoustic noise and vibration effects[2]. An argon ion laser source was employed in a Fizeau interferometer structure and this technique was proven to be effective in eliminating undesired vibration effects. A recent development for dynamic WLI measurement is the 4D microscopy employing high speed camera and FPGA for real time image processing[3].

In recent years，many methods have been developed for measuring vibratory modes of micromechanical devices，such as MEMS and MOEMS with fiber optic interferometry[4-5] or single-beam laser Doppler vibrometers[6]. The major disadvantage of these techniques is that its point-type measurement requires lateral scanning，which is extremely

time consuming. To address this, measurements of in-plane vibrations of MEMS, with nanometer resolution, have been achieved by using the correlation of synchronous images[7]. Meanwhile, for out-of-plane measurement, laser phase-shifting interferometry can also be combined with stroboscopic lighting[8-9] for measuring the surface of vibrating M(O)EMS. De Groot [9] has performed an approximate simulation study on the effect of pulse duty cycle on stroboscopic white light interferometry (SWLI) measurement. Pettitgrand and Bosseboeuf[10] have also reported a comprehensive study of the effect of duty cycle to contrast degradation and error of profile measurement for stroboscopic phase shifting interferometry system. Chen et al.[11] have developed a signal deconvolution technique for improving the contrast of the interferogram acquired at a long-pulse duty cycle. Since then, SWLI has been widely investigated for various applications in optical precision metrology.

## 1 Optical system configuration of SWLI

Figure 1 shows theschematic diagram of the developed optical system using a Michelson or Mirau interferometric objective for the full-field stroboscopic interferometry measurement[11-13]. In the optical system, the incident light from the light source module is collimated by a set of optical lenses to produce a parallel white light beam that illuminates the measured surface and the reference mirror. The system was equipped with a single super luminescent light-emitting diode (SLED). When incorporated with a developed synchronous light control module, the SLED can be driven in pulsed or continuous wave modes. This arrangement enables a dual-mode measurement capability in a single interferometer, where the continuous white light source can be applied for static surface profilometry while the stroboscopic light source is utilized for dynamic vibratory measurements[14].

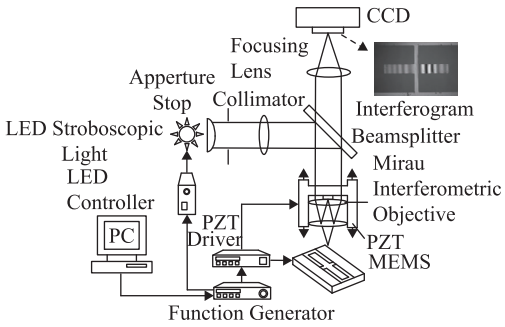


Figure 1 Schematic diagram of the developed optical system

In addition, for thevertical translation required in white-light interferometric scanning, a piezoelectric system equipped with a capacitive positioning sensor for closed-loop control has a 100 μm vertical translation range and a sub-nanometric resolution. The hardware setup of the developed optical system is shown in Figure 2.

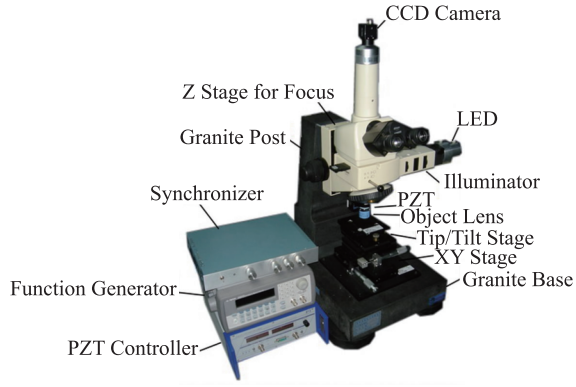


Figure 2 A microscopic optical system developed for dynamic measurement

In general, vibratory motionundermines the contrast quality of conventional interferometric fringe images. To avoid this, stroboscopic source illumination and signal synchronization are developed for capturing repeated images of the sample at the identical phase of oscillation, so that the interference fringes acquired are unambiguous. Figure 3 is the schematic diagram of a system for detecting out-of-plane displacement and identifying resonant frequency. The system comprises a central control unit, a synchronous control unit, a vibration-driving unit, a light-emitting unit and an image-acquiring unit. The central control unit is coupled to the synchronous control unit and the image-

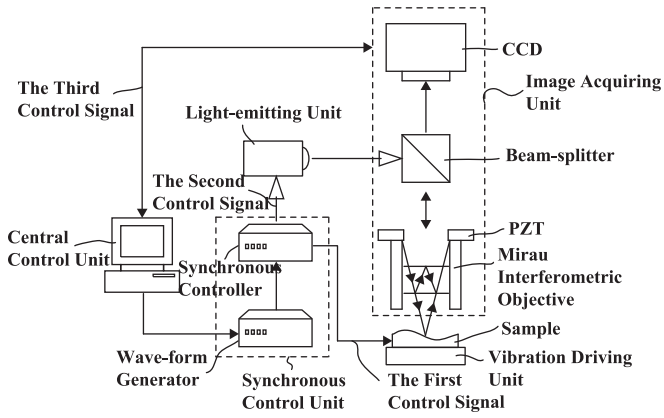


Figure 3 Schematic diagram showing the developed apparatus for identifying an out-of-plane displacement characteristic and a resonant frequency

acquiring unit. The central control controls the synchronous control unit and the image-acquiring unit by its embedded software. The synchronous control unit comprises a wave-form generator and a synchronous controller. Upon receiving a request from the central unit, the wave-form generator produces the control signal, which can be a pulse, a sine-wave or a square-wave. Using the control signal generated by the wave-form generator, the synchronous control unit generates synchronously the first control signal, the second control signal and the third control signal.

The vibration-driving unit carries the tested MEMS component or system and vibrates it upon receiving the first control signal. The vibration-driving unit is a piezoelectric element (PZT) for vibration generation. The SLED is coupled to the synchronous control unit and generates a stroboscopic flash upon receiving the second control signal. Compared with conventional laser sources, the SLED consumes relatively less energy, thus avoiding damage to micro elements due to potential overheating. Moreover, the SLED can be installed in a general microscopic interferometry. Without the use of laser as in laser-Doppler anemometry, the developed apparatus is less complex and incurs much lower manufacturing cost.

To achievesynchronous image acquisition, the image-acquiring unit is coupled to the central control unit. Upon receiving the third control signal, the unit acquires an interference image from the sample and transmits the interference image acquired to the central control unit. The unit comprises a lens module, a beamsplitter and a charge coupled device (CCD). The lens module comprises a driver for controlling an interference objective to perform scanning interferometric measurement for surface profilometry. The beamsplitter receives the stroboscopic flash to guide the light into the lens module and then projects the light onto the vibrating sample. It further receives the light reflected from the vibrating sample to generate an interference pattern. The interference pattern corresponding to the vibrating sample is acquired by the CCD to form the interference image, which is later transmitted to the central control unit for image analysis.

## 2 Theoretical modeling of SWLI

The intensity of the interferometric fringe in an arbitrary region of the object under test can be expressed as[1,11-12]:

$$I(z) = I_0[1 + C(z)\cos(k(z - z_0) + \phi_0)] \quad (1)$$

where $I(z)$ is the interferometric light intensity that varies with the position $z$ of the surface under test; $I_o$ is the mean interferometric light intensity; $C(z)$ is the interference contrast; $k = \frac{2\pi}{\lambda}$ is the wave number of the light source; $z_0$ is the position of zero optical difference; and $\phi_0$ is the phase offset of the interferogram.

When the object under test is vibrating as a sinusoidal function with anamplitude $\Lambda$, frequency $\omega$, and phase $\varphi$, the vertical position of zero optical difference $z_0$ can be expressed as:

$$z_0(\omega, t, \Lambda) = z_e + \Lambda\sin(\omega t + \varphi) \quad (2)$$

where $z_e$ is the equilibrium position of the vibration.

Assuming that the frequency of the vibration is much higher than the scanning speed of thepiezoelectric transducer (PZT) used for vertical scanning, the position $z$ does not change during the interferogram capturing process. Therefore, the position $z$ in Eq. (1) can be regarded as time invariant and a new variable, $z'$, can be defined as follows:

$$\begin{aligned} z'(\omega, t, \Lambda) &= z - z_o(\omega, t, \Lambda) \\ z'(\omega, t, \Lambda) &= z - z_e - z_v(\omega, t, \Lambda) \end{aligned} \quad (3)$$

where $z_v = \Lambda\sin(\omega t + \varphi)$.

By substituting Eq. (3) into Eq. (1), Eq. (1) can be rewritten as follows:

$$\begin{aligned} I(z'(\omega, t, \Lambda)) = I_0[1 + C(z'(\omega, t, \Lambda)) \\ \cos(k(z'(\omega, t, \Lambda)) + \phi_0)] \end{aligned} \quad (4)$$

In SWLI, the light pulse is usually represented by a perfect delta function synchronized with the vibration signal. For a short duty cycle, the vibrating object under test is in the static interference mode; therefore, the measurement can be regarded as a static interference measurement. However, in actual condition, the pulse of stroboscopic lighting, such as LED, is not a delta function and is more likely to be represented by a Gaussian function as follows:

$$P(t) = P_c e^{\frac{-(t - t_c)^2}{2\delta_t^2}} \quad (5)$$

where $\delta_t$ is the standard deviation of the stroboscopic pulse; $P_c$ is the maximum light intensity; and, $t_c$ is the center of the stroboscopic pulse, which is a time delay of the pulse that can be adjusted at different phases of vibration.

The physical meaning of the pulsed light in

stroboscopic interferometry is emitted at different height positions of the vibrating object imaged by the camera. Therefore, the light pulse can be transformed and expressed by the height of the tested object as follows:

$$P(z'(\omega,t,\Lambda)) = P_c e^{\frac{-(\frac{1}{\nu}(z'(\omega,t,\Lambda)-z_c))^2}{2\delta_{z\tau}^2}} \quad (6)$$

where $z_c$ is the center position of the sample associated with the pulse center; $\delta_{z\tau}$ is the light intensity distribution along the $z$ axis; and, $\nu$ is the vibrating speed of the object under test ($\nu = A\omega\cos(\omega t + \varphi)$).

The interference light beam, $I_s$, can be regarded as the output of the convolution operation between the stroboscopic pulse $P(z(\omega,t))$ and the vibratory interferometric light intensity of a vibratory object under test, $I(z,k,t)$. Thus, $I_s$ can be represented as follows:

$$I_s(z'(\omega,t,\Lambda)) = I(z'(\omega,t,\Lambda)) \otimes P(z(\omega,t)) \quad (7)$$

For the case of WLI where broadband light source is employed, the captured interferogram comprises interferograms from the entire constituent wavelength. Thus, Eq. (4) can be rewritten as the integration of all interferograms as follows:

$$I(z'(\omega,t,\Lambda),k) = \int_{k_0}^{k_n} I_0[1 + C(z'(\omega,t,\Lambda)) \cos(k(z'(\omega,t,\Lambda)) + \Delta\phi)]dk \quad (8)$$

where $k_o$, $k_n$ are the beginning and ending wave numbers of the reflective light from the tested object surface, in which these two parameters depend on the wavelength dependence of the reflection coefficient of the tested surface.

Equation (8) represents the intensity of the interfered light beam, which is a function of the wavelength of both light and time. The actual measured vibratory interferometric signal of SWLI can be formulated as:

$$I_s(z'(\omega,t,\Lambda),k) = \left[\int_{k_0}^{k_n} I_0[1 + C(z'(\omega,t,\Lambda)) \cos(k(z'(\omega,t,\Lambda)) + \phi_0)]dk\right] \otimes [P_c e^{\frac{-(\frac{1}{\nu}(z_e+z_1(\omega,t)-z_c))^2}{2\delta_{z\tau}^2}}] \quad (9)$$

The intensity of the interfered light beam is captured during the pulse time of the stroboscopic light and integrated alongthe exposure time of the imaging sensor. The interferograms are captured when stroboscopic lighting is activated during the duty cycle of the LED ($\delta t$). The integration process intends to blur the interferograms when the duty cycle is increased. With the pulse length ($\delta t$) of the light beam taken into account, Eq. (9) can be rewritten as:

$$\begin{aligned} I_s(z'(\omega,t,\Lambda),k) &= \int_{\theta_0}^{\theta_0+\delta t} I_s(z'(\omega,t,\Lambda),k) \otimes P(z(\omega,t))\, \mathrm{d}t I_s(z'(\omega,t,\Lambda),k) \\ &= \int_{\theta_0}^{\theta_0+dt} \left\{ \left[\int_{k_0}^{k_n} I_0[1 + C(z'(\omega,t,\Lambda)) \cos(k(z'(\omega,t,\Lambda)) + \phi_0)]\mathrm{d}k\right] \otimes [P_c e^{\frac{-(\frac{1}{\nu}(z_e+z_1(\omega,t)-z_c))^2}{2\delta_{z\tau}^2}}] \right\} \mathrm{d}t \end{aligned} \quad (10)$$

where $\theta_0$ is the initial time of the stroboscopic pulse corresponding to the phase delay of the pulse with respect to the sinusoidal vibration and $\delta t$ is the length of the stroboscopic pulse (also called cycle time).

Taking into account the effect of numerical aperture (N. A.) of the interferometric objective to the formed interferogram, Eq. 10 can be rewritten as:

$$I_s(z'(\omega,t,\Lambda),k) = \int_{\theta_0}^{\theta_0+dt} \left[\int_{k_0}^{k_n}\int_{0}^{\varphi_n} \{I_0[1 + C(z'(\omega,t,\Lambda)) \cos(k(z'(\omega,t,\Lambda))\cos\varphi + \phi_0)]\sin\varphi\cos\varphi d\varphi\}\, dk\right] \otimes [P_c e^{\frac{-(\frac{1}{\nu}(z_e+z_1(\omega,t)-z_c))^2}{2\delta_{z\tau}^2}}] dt \quad (11)$$

where $\varphi_0$ is the half angle of the maximum cone of the light that can enter or exit the objective lens.

## 3 Influence of stroboscopic light to accuracy of dynamic measurement

Since thestrobed white light has its unavoidable pulse length, a study is necessary to verify the effect induced by the physical phenomenon of cycle time of strobed white light on the accuracy of dynamic characterization[1,12,14]. The duty cycle effect in SWLI can be evaluated by comparing simulation results obtained from the mathematical model with actual measurements made experimentally. For this, a simulation data is generated by using the mathematical model of a SWLI system. The model is validated with experimental data obtained using a sample with pre-calibrated system characteristics. Analysis is provided to illustrate the relationship between the lighting phase and measured deviation and also the correlation between the

cycle time and measured errors.

### 3.1 Experimental Setup and Design

Figure 4(a) shows the setup of a general Mirau-based SWLI system. As can be seen, it comprises a white light LED as the light source for generating stroboscopic lighting for the system. The light is controlled by the pulse from function generator 1, and directed by a beamsplitter to a Mirau interferometric objective attached on a PZT for performing vertical scanning. In the experiment, the magnification of the objective employed is 20X and its numerical aperture (N. A.) is 0.4. The sample is vibrated by a sinusoidal signal generated by function generator 2. The key element of the setup is accurate synchronization between the two function generators to ensure consistency of the phase difference between the pulse signal of the LED and the sinusoidal signal of the vibrating sample. The stroboscopic phase shift is performed by changing the phase delay between the sine wave and the stroboscopic pulse generated by the function generators.

Figure 4(b) shows the synchronization between the pulse signal of the LED ($\delta t$), vibration of the sample and the exposure time of the camera ($T_{exp}$). The exposure time of the camera ($T_{exp}$) is usually set to be much higher than the light pulse, so that the image is an integration of many frozen interferograms. Phase delay between the vibration signal and the pulse signal ($\theta_i$) is varied to enable reconstruction of the vibrational mode of the sample. An example of phase delay is shown in Figure 4(b), in which phase delay $\theta_1$ is applied to the pulse signal for reconstruction of the object at 0° while phase delay $\theta_2$ is employed to perform reconstruction of the object at 90°. By applying different phase delays between pulse and vibration signal in one period, the vibrating object can be reconstructed and the dynamic characteristic of the object when excited by a periodical signal can be observed. This principle can be applied for analyzing vibrating objects both for in-plane and out-of-plane directions.

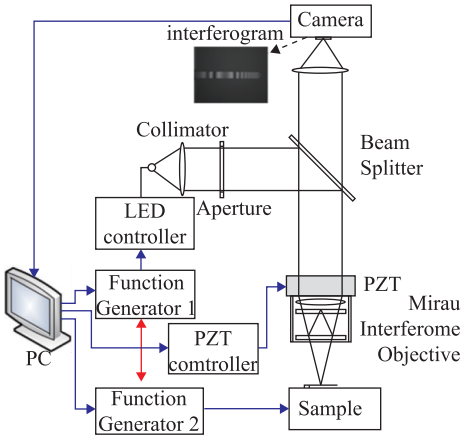


(a) system setup for the SWLI system

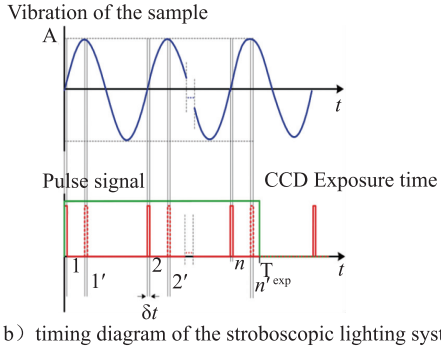


(b) timing diagram of the stroboscopic lighting system

Figure 4　Illustration of the SWLI and its timing control

In the experiment, the vibratory movement of the sample is measured at several different phase delays, namely 0°, 90°, 180° and 270° since these four phases have different characteristics in sinusoidal vibration. Movement speed of the sample reaches its minimum at phases of 90° and 270° and reaches its maximum at the equilibrium point where the phase is 0° and 180°. On the other hand, the deflection of the sample reaches its maximum at the phase of 90°, minimum at the phase of 270° and at the equilibrium point when the phase is 0° and 180°.

In the SWLI, the duty cycle of the light pulse has to be maintained as short as possible. However, in some cases, this condition cannot be satisfied due to limitation of the lighting physics. Therefore, experiments and simulations are performed to observe the effect of the long duty cycle. In the study, simulations are performed with duty cycles at 1%, 5%, 10%, 15%, 20% and 25%. Real spectrum of the white light LED light source and spectral response of the CCD camera are measured and characterized in advance, and then employed to generate the simulated interferogram. The same light source is employed in both simulation and experiment to avoid generating any potential difference. The LED employed in the experiment is a phosphor-type white LED and the after-glow time has been reported in[12]. Figure 5 illustrates the spectrum of the LED (shown by line (a) on the chart) and the wavelength sensitivity of the CCD (shown by line (b) on the chart) employed in the

developed stroboscopic WLI system, respectively. The spectrum shows that the CCD is more sensitive at around 500 nm and less sensitive at other wavelengths. This sensor characteristic changes the light distribution of the LED by making the blue light peak at 450 nm weaker and the green light peak more dominant. Hence, the light spectral distribution can be reasonably approximated by the combined spectral response (shown by line (c) on the chart).

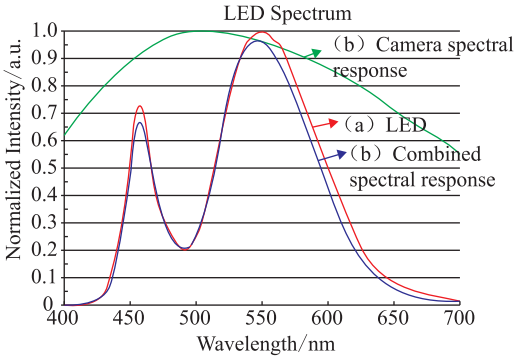


Figure 5 (a) Spectrum of the white light LED light source; (b) relative sensitivity of the CCD camera employed in the system; and (c) spectrum of the light source used in the simulation as an approximation of the intensity captured by the CCD

The WLI signal obtained from both simulation and experiment are shown in Figure 6, in which duty cycle of the pulse light is 1% and the phase of the vibration is 90°. In the figure, the intensity values are intentionally separated at two different levels.

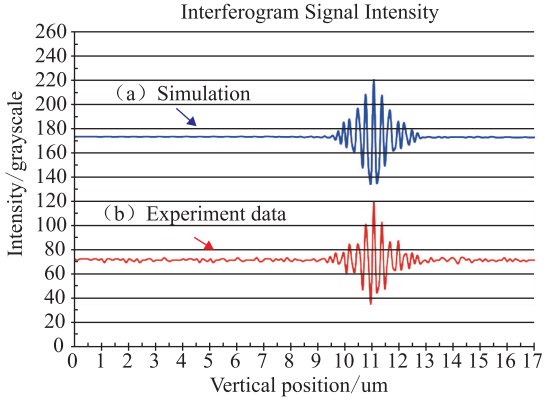


Figure 6 WLI signal generated from simulation and experiment, in which a vertical offset is intentionally added to separate the two lines

Figure 7 shows an AFM cantilever microbeam used in both simulations and experiments. Its detailed material specifications are displayed in Table 1. With the beam assumed to be rigidly clamped at one end, the flexural resonant frequencies of a cantilever beam having a cross-section $A$ and an inertial moment $I$ can be theoretically derived. When taking the tip mass into account and assuming the tip to be a cone whose height and base diameter are both $h$, the authors modeled the corrected flexural resonant frequencies of a cantilever beam as follows[14]:

$$f_{corr} = \frac{\sqrt{3}}{2\pi}\sqrt{\frac{EWT^3}{12(PL^3 + 0.236pL^4)}}$$

$$= 0.276\sqrt{\frac{EWT^3}{\rho(\pi H^3 L^3 + 2.832\ WTL^4)}} \quad (12)$$

where $W$ is the width of the cantilever beam; $T$ is the thickness of the cantilever beam; $P$ is the mass of the tip; $p$ is the cantilever mass per unit-length; and $H$ is the tip height of the cantilever beam.

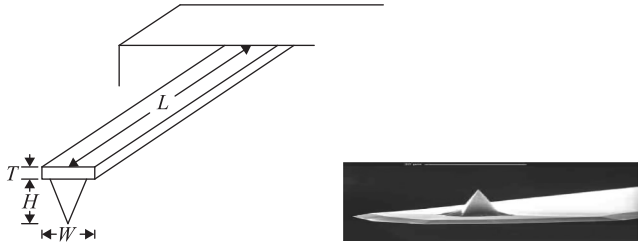


(a) schematic diagram (b) actual micro beam

Figure 7 Tested AFM cantilever microbeam

Table1 Dimension specifications of the tested contact-mode AFM cantilever microbeam

| Technical Data | Value |
|---|---|
| Type | Contact Mode |
| Thickness | $1.8 \times 10^{-6}$ m |
| Width | $46 \times 10^{-6}$ m |
| Length | $446 \times 10^{-6}$ m |
| Density | 2330 kg/m$^3$ |
| Young's modulus | $1.69 \times 10^{11}$ N/m$^2$ |
| Shear modulus | $0.5 \times 10^{11}$ N/m$^2$ |
| Poisson's Ratio | 0.069 |

Vibration is simulated according to Eq. (3) with vertical amplitude of 0.837, 0.926, and 1.202 um at a frequency of 80.778 kHz, which is exactly the second measured resonant mode of the tested object. With these simulation parameters, the interferogram of the sample can be generated at different phases and duty cycles. Height of the tested object can be detected and reconstructed from the interferogram signal using the SEST algorithm[15], which is

also implemented in the developed SWLI system in the experiment.

### 3.2 Experimental results and analyses

**3.2.1** Vibratory cantilever profiles reconstructed at 1% duty cycle

In practice, since the duty cycle cannot be set to zero in experiments, it can only be set to be as small as possible for minimizing the effect of duty cycle. A lighting duty cycle set at 1% for observing a cantilever beam vibrating at a frequency of 80.778 kHz has a light pulse length equal to 124 ns, which reaches to the physical limit of the white light LED. The maximum vertical movement during the duty cycle at the maximum vibratory speed is 1% of the vibratory amplitude. Thus, the duty cycle set at 1% is taken as a reference for comparison with other higher duty cycles for verifying impacts on measurement accuracy.

Figure 8 shows the measurement results of the vibrating cantilever beam with the duty cycle set at 1% and three vibration amplitudes of 0.837, 0.926, and 1.202 μm

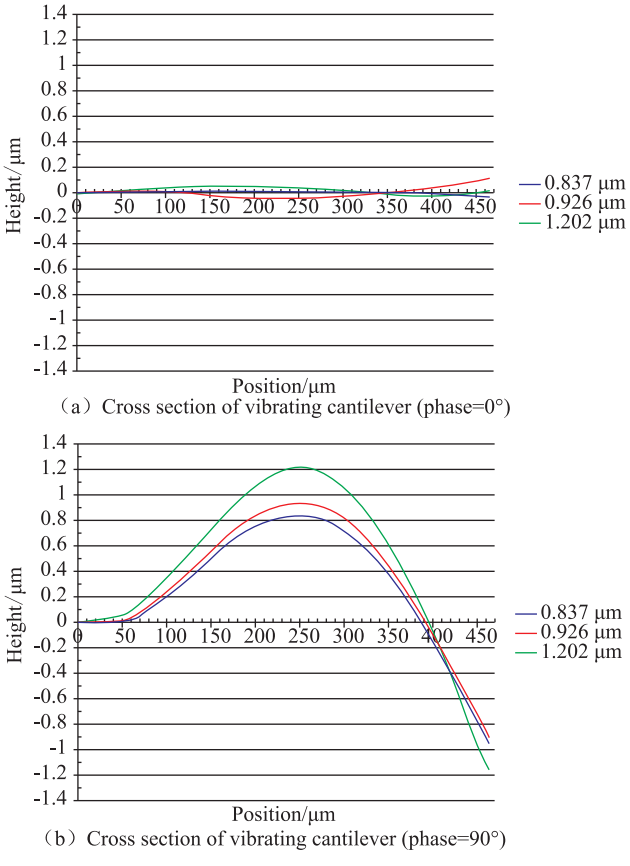


(a) Cross section of vibrating cantilever (phase=0°)

(b) Cross section of vibrating cantilever (phase=90°)

Figure 8 Dynamic profile reconstruction of vibrating cantilever beam and cross-sections at phase delays of 0° and 90° (the profiles shown here are only emphasized on the cantilever beam)

respectively. To highlight the variations during vibration, the surface profiles shown are only of the vibrating cantilever beam without the static parts of the sample. A Median filter with a $5 \times 5$ pixel window was applied to the reconstructed profiles for removing some minor scattered noises. These measured cantilever profiles at two specific phases were employed in this study as the reference.

**3.2.2** Degradation of fringe contrast

Another parameter that can be observed from the measurement results is the variation of fringe contrast with different duty cycles. Theoretically, the fringe becomes blurred with a larger duty cycle due to the averaging of interferograms taken at several height positions. In the study, the contrast in the middle of the cantilever beam where the deflection of the beam reaches its maximum is analyzed. The contrast value can be calculated from the modulation of the interferogram images using the following formula:

$$C_i = \frac{I_{\max} - I_{\min}}{I_{\max} + I_{\min}} \tag{13}$$

where $I_{\max}$ and $I_{\min}$ are the maximum and minimum intensity of the interferogram, respectively.

Figure 9 shows the comparison between experimental results and theoretical data generated using the developed mathematical model with the same vibration frequency and amplitude as the one applied in the experiment. Variations in interferogram contrast are examined under two conditions, when the cantilever beam is at its maximum speed, i.e., at phase delays of 0° and 180°; and when the cantilever beam is at its minimum speed, i.e., at phase delays of 90° and 270°. Data from phase delay of 0° and 90° are used to represent the two conditions. As can be seen, experimental results and simulation data show similar trends. Interferogram contrast is rapidly degrading when the duty cycle turns larger. Moreover, the contrast at phase delay of 0° is degrading more rapidly than that at phase delay of 90°. Despite having similar trends, the experimental data in general show a slightly lower contrast than the theoretical (simulated) results. Such difference can be accounted for the increase of cycle time of the strobed lighting or the light exposure time of the image acquiring device, such as the CCD camera. Simulation model for image sensing is not constrained by such physical limitation and should be more accurate than the actual measurement in the experiment.

Nevertheless, in theory, a higher fringe contrast does not always guarantee higher accuracy in measurement of the vibrating surface than a lower one because the SWLI quantifies the surface height by detecting on the zero optical path difference (OPD) instead of image contrast directly.

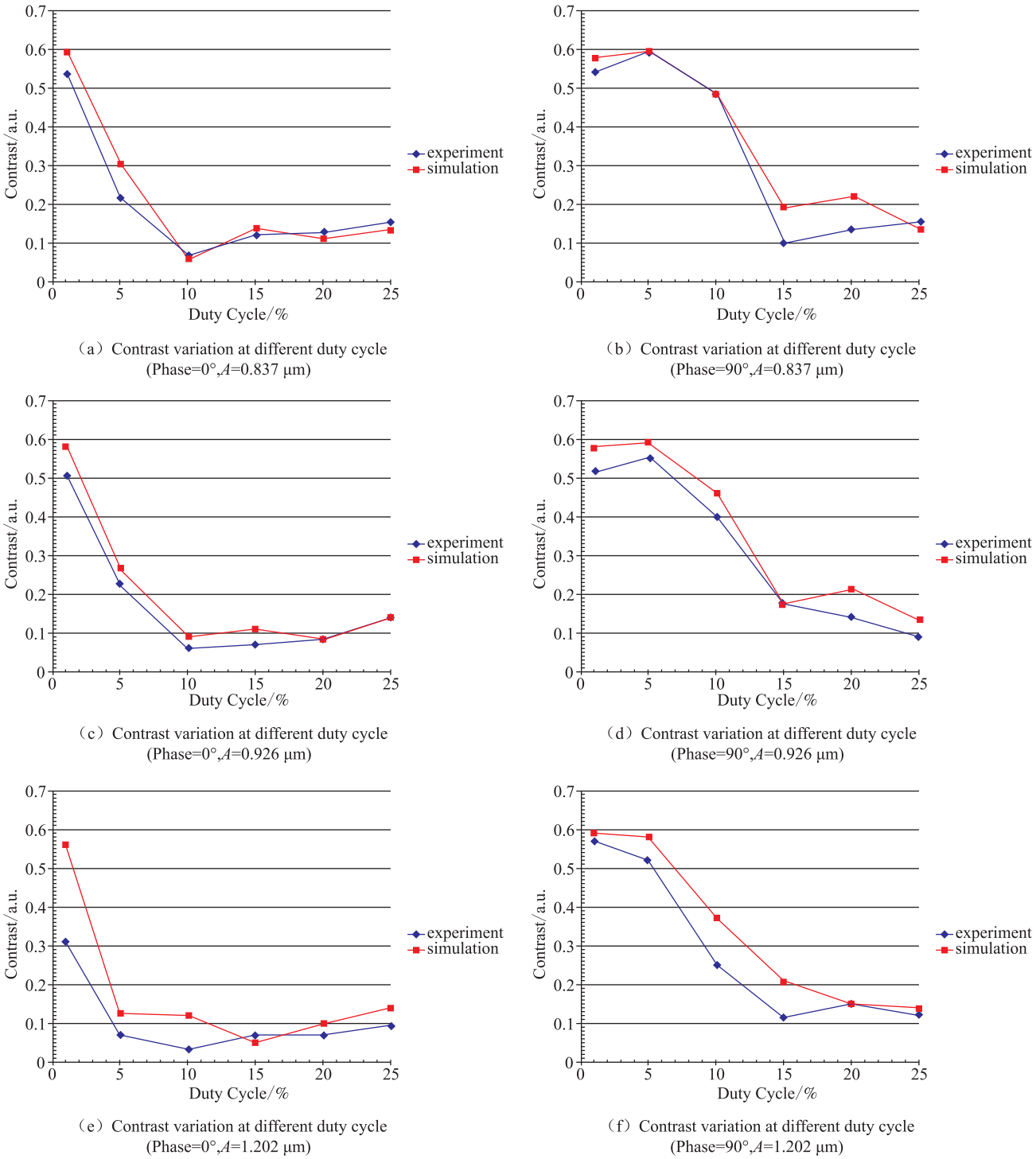


(a) Contrast variation at different duty cycle (Phase=0°, $A$=0.837 μm)

(b) Contrast variation at different duty cycle (Phase=90°, $A$=0.837 μm)

(c) Contrast variation at different duty cycle (Phase=0°, $A$=0.926 μm)

(d) Contrast variation at different duty cycle (Phase=90°, $A$=0.926 μm)

(e) Contrast variation at different duty cycle (Phase=0°, $A$=1.202 μm)

(f) Contrast variation at different duty cycle (Phase=90°, $A$=1.202 μm)

Figure 9 Interferogram contrast variation with different duty cycles for an amplitude of 0.837, 0.926, 1.202 μm respectively

**3.2.3** Accuracy of dynamic profile measurement

The dynamic surface profiles were then measured by the developed SWLI experimental setup. Theoretical simulation was also performed to obtain the out-of-plane

displacement from the mathematical model. Before measurement accuracy analysis, the measurement data from the experiments were first subtracted from the static profile of the microbeam to obtain the *z*-axis vibratory displacement of the microbeam. The static profile is calculated from the average height from the profile measured at phase delay of 90° and 270°. Then, an arbitrary point on the surface of the sample, which has an initial phase of zero, can be taken as a reference for observation of the vibratory height variation of the microbeam. Figure 10(a) – (c) shows the comparison of

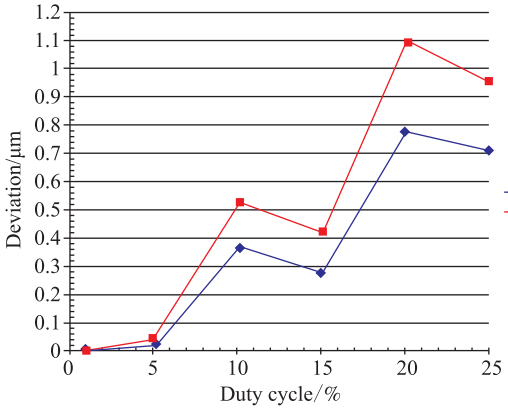


(a) Comparison between simulation and experiment (Phase=0°, $A$=0.837 μm)

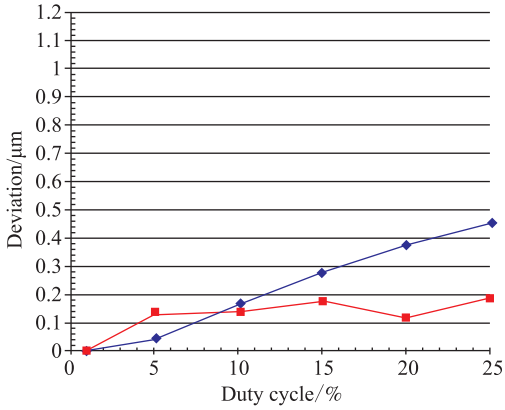


(b) Comparison between simulation and experiment (Phase=90°, $A$=0.837 μm)

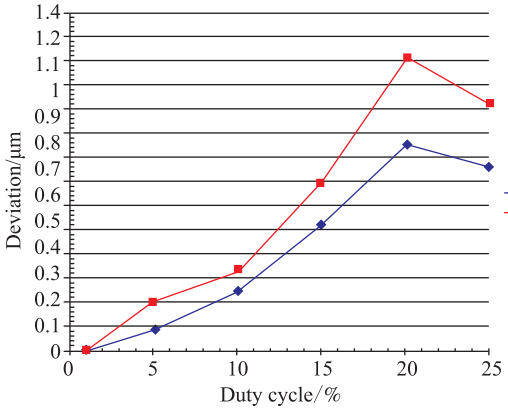


(c) Comparison between simulation and experiment (Phase=0°, $A$=0.926 μm)

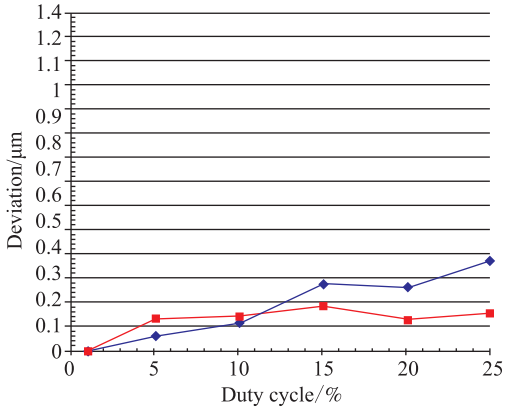


(d) Comparison between simulation and experiment (Phase=90°, $A$=0.926 μm)

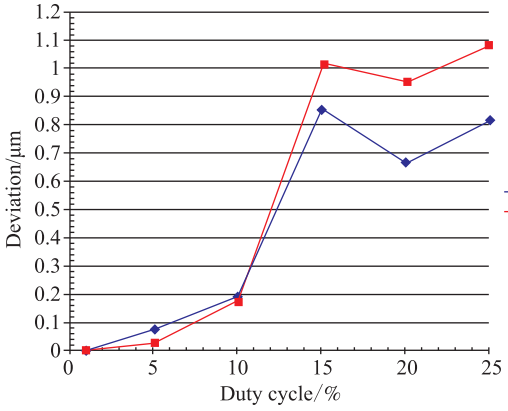


(e) Comparison between simulation and experiment (Phase=0°, $A$=1.202 μm)

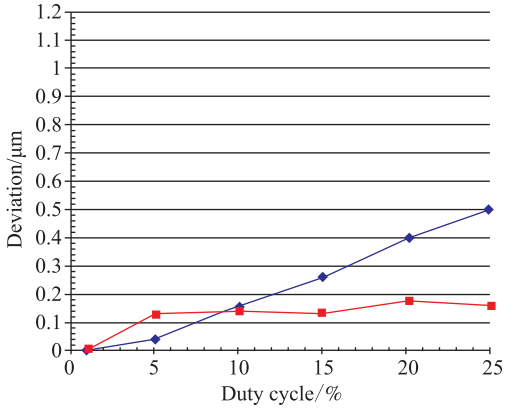


(f) Comparison between simulation and experiment (Phase=90°, $A$=1.202 μm)

Figure 10　Comparison in height measurement between simulation and experimental results at amplitude of 0.837, 0.926, 1.202 μm respectively, in which the deviation is calculated relative to the measured deflection of cantilever beam at 1% duty cycle for the simulation and the experimental data, respectively.

measured deviation between simulation and experimental results obtained when the phase delay is 0° and 90°, respectively. The deviation is calculated relative to the measured deflection of cantilever beam at 1% duty cycle. As seen in Figure 10(a) – (c), the simulation and experimental results have a reasonably close trend in out-of-plane measurement within 25% of duty cycle time. This indicates that the simulation model developed here can provide a reasonable prediction on measurement deviation caused by the effect of duty cycle. The averaged difference between simulation and experiment data is less than 15.4% of the vibrational amplitude when the duty cycle is below 15%.

Furthermore, difference in height measurement between simulation and experimental results are illustrated in Figure 11 (a) and (b) by using percentage of the vibratory amplitude. The results further quantify the difference between simulation and experiment by employing three different vibration amplitudes. For 0° phase delay, the maximum difference for three tested amplitudes is 38.4% and the averaged deviation is 15.4%. Compared with 0° phase delay, the maximum difference for 90° phase delay in the three tested amplitudes is slightly decreased to 31.9% while the averaged deviation is 11.7%. As seen in Figure 11 (a) and (b), it is clear to see that the deviation between the simulation and the experiment from three different vibration amplitudes shows a close trend when the duty cycle is increased. It is important to note that the large deviation can be explained by the increase of cycle time of the strobed lighting or the light exposure time of the image acquiring device, which is not sufficient to capture the moving microbeam in the vicinity of 0° phase delays. The measurement errors with duty cycle are presented in Figure 11 (c) and (d), it can be seen that the measurement err orisapproxi mately increased in trend with the duty cycle.

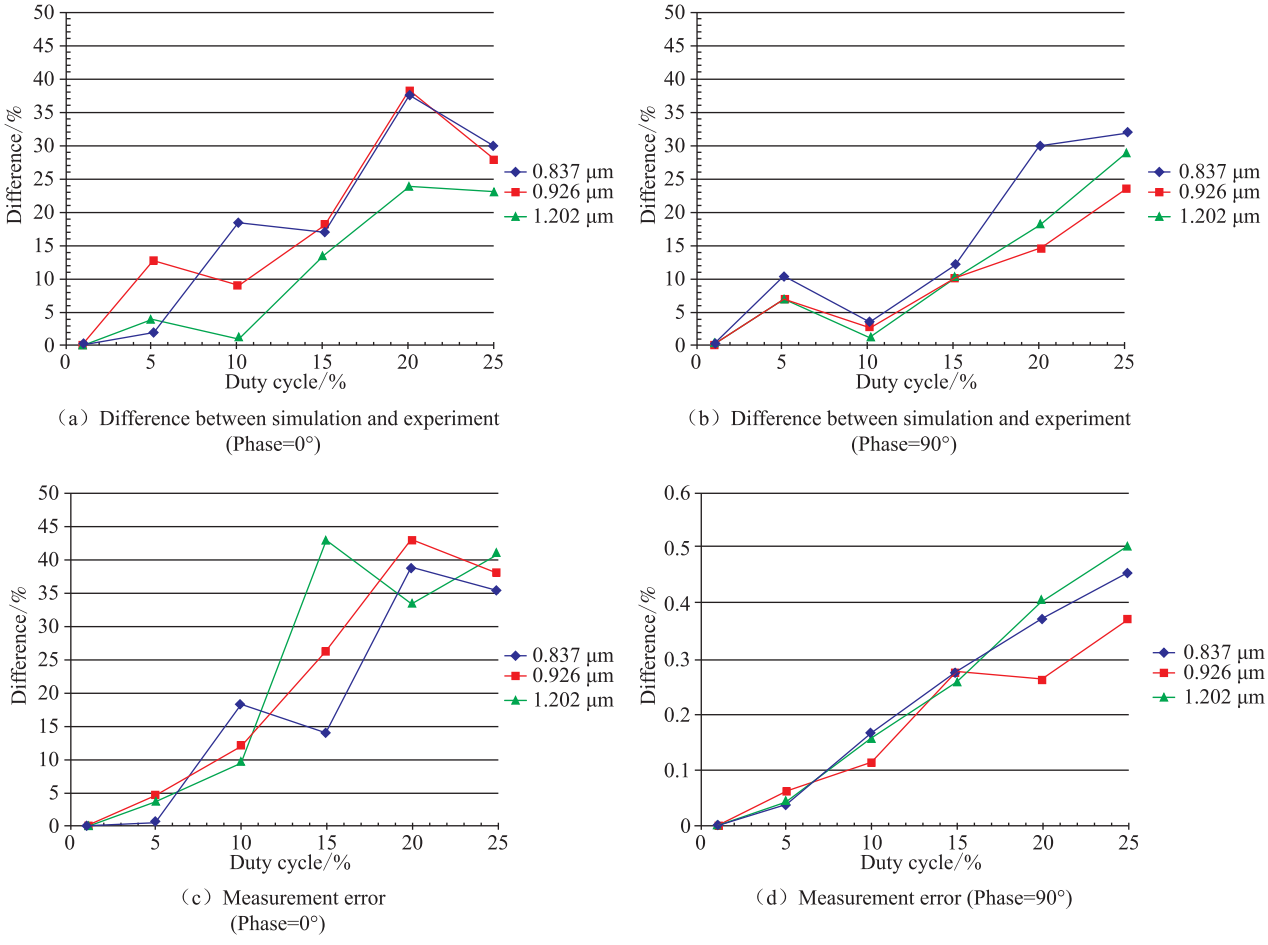


(a) Difference between simulation and experiment (Phase=0°)

(b) Difference between simulation and experiment (Phase=90°)

(c) Measurement error (Phase=0°)

(d) Measurement error (Phase=90°)

Figure 11 Difference between simulation and experiment for (a) phase delay at 0° and (b) phase delay at 90°, in which the value is calculated on the difference between the simulation and the experimental data; (c) measurement error for phase delay of 0°; and (d) 90°

Measurement was performed three times for each cases and the standard deviation of the error for all measurement case are kept within 100 nm. The reason why measurement was only performed three times for each case is to shorten measurement time as it is very sensitive to environment disturbance. The error trend for phase delay of 90° is less fluctuated than the one with phase delay of 0°. This is reasonable as the vibratory speed for phase delay of 90° is much smaller than the one for 0°.

From the simulation model, the contrast of the interferogram and out-of-plane of the SWLI can be predetermined accurately and compared with the measured data which is affected by the duty cycle. Again, error estimation and compensation can be implemented to correct the measured errors of the SWLI. However, the developed model may still have some limitations since optical parameters are not fully accommodated in the developed mathematical model. The behaviors of the optical components inside the microscope are not fully taken into account in the mathematical model because of practical difficulties in characterizing and measuring the microscope optical parameters. These behaviors may include spectrum response of the optical components against the light source, LED spectral shift[16], dispersion of the Mirau objectives, which has been reported as one of the problems in white light interferometry[17]. Moreover, the simulation assumes that the interferogram is formed in ideal condition without dispersion of the optical components. However, correction of these factors may be needed for establishment of even more accurate mathematical modeling for SWLI in evaluation out-of-plane displacement.

## 4 Automatic resonant frequency detection[12-13]

In general, when the vibratory frequency reaches its resonant peak, the interferogram will show the following three major characteristics.

①The vibratory motion is periodical; ②The vibratory amplitude reaches its maximum; ③ The vibratory nodal lines are located at the corresponding fixed positions.

Figure 12 shows the results of resonance detection of an AFM cantilever beam initially leveled at a horizontal orientation and then vibrated at two different modes (a non-resonant frequency mode and a resonant frequency mode shown in Figure 12(a) and Figure 12(b), respectively). The following important facts can be extracted from the results obtained.

1) Owing to increase in vibrating amplitude, the interferogram image acquired from a vibration frequency closer to its resonant mode generally contains more high-frequency components in its frequency domain.

2) The image focus (contrast) of theinterferogram image is enhanced when the vibration is shifted towards its resonant frequency and reaches its peak as the vibratory frequency is set exactly on one of the resonant modes.

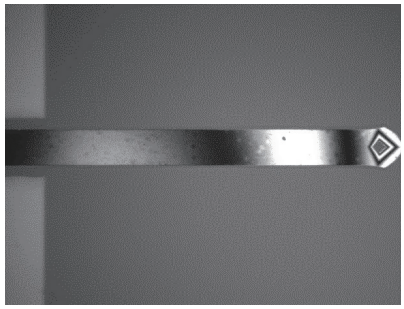

(a) The interferometric fringe acquired by the stroboscopic method when the cantilever vibrated at a vibratory frequency of 200 kHz, which was close but not on its secondary resonant mode

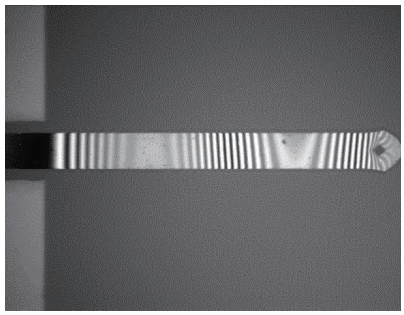

(b) The interferometric fringe acquired by the stroboscopic method when the cantilever vibrated at a vibratory frequency of 205 kHz, which was exactly on its secondary resonant mode

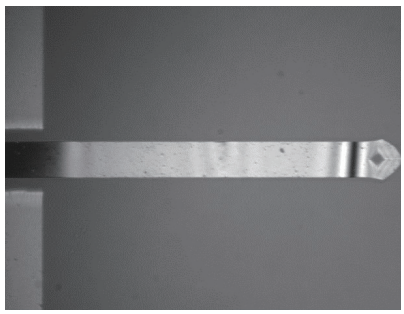

(c) The interferometric fringe acquired by the time averaged method when the cantilever vibrated at a vibratory frequency of 205 kHz, which was exactly on its secondary resonant mode

Figure 12 The white-light stroboscopic interferogram images of measuring an AFM contact-mode cantilever beam

To demonstrate the above physical phenomenon, the interferogram images displayed in Figs. 12 (a) and (b) were transformed into corresponding images in the frequency domain, shown in Figs. 13(a) and (b), respectively. Comparing the two figures reveals that more high-frequency components can be observed in Figure 13(b). In view of this phenomenon, an automatic resonant mode detection method, which measures the variations in interferometric fringe density, is proposed for dynamic characterization of MEMS.

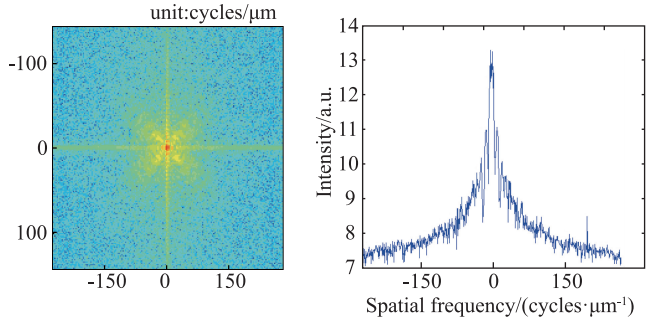


(a) Vibrating at a vibratory frequency of 200 kHz, which was close but not exactly on its secondary resonant mode and it was measured by the stroboscopic method

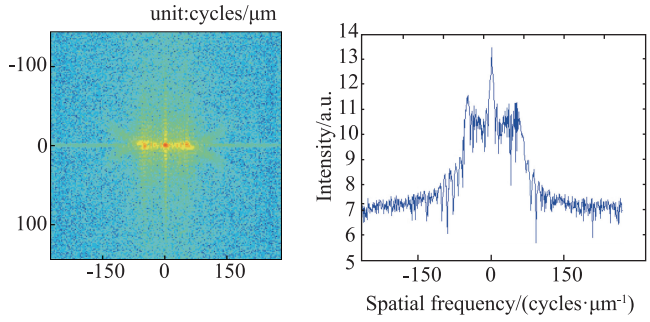


(b) Vibrating at a vibratory frequency of 205 kHz, which was exactly on its secondary resonant mode and it was measured by the stroboscopic method

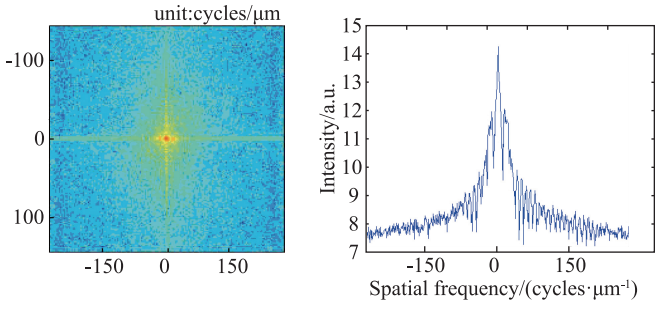


(c) Vibrating at a vibratory frequency of 205 kHz, which was exactly on its secondary resonant mode and it was measured by the time-averaged method

Figure 13 Fourier transform diagram of the interferogram image obtained by measuring an AFM contact-mode cantilever beam

Figure 14 is a flow chart showing the method for resonant frequency identification. A MEMS component serves as the sample to be examined. First, the component is leveled at its horizontal position and a scanning frequency range including a series of scanning frequencies is set by the central control unit. The scanning frequency range can be set from 1 kHz to several MHz at an adequate frequency interval, such as 0.1 kHz or smaller according to the scanning resolution required. Following this, a scanning frequency is first chosen and checked against the pre-set scanning frequency range. If it is within the pre-set range, the method proceeds onto the next step for determining a vibrating frequency of the sample. When the stroboscopic interferogram image is effectively frozen, the image is then acquired. An effective noise filtering algorithm, such as low-pass filtering, is employed to remove the image noises being generated from unexpected dust particles left on the test component's surface or other resources. Furthermore, the image is normalized to minimize gray-level variances caused by possible fluctuations in intensity of the SLED light source.

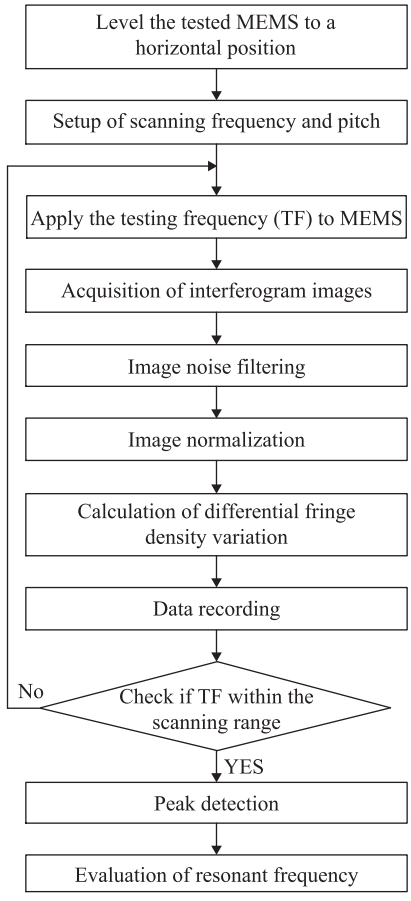


Figure 14 Flow chart of the automatic resonant frequency detection

As demonstrated in Figs. 12 and 13, measuring the variation in fringe density of stroboscopic interferogram images can effectively detect resonant peaks and identify the corresponding vibration modes. Variation in fringe density is directly associated with changes in image contrast since the spatial frequency of fringes affects the degree of image contrast. Functions of image contrast are evaluated assuming that contrast of images is enhanced with improvement in focus. Changes in image contrast can be described mathematically by the magnitude of the high frequencies or gradients; standard deviation of pixel intensity; or autocorrelation. Among these methods, Vollath's F4 based on autocorrelation was found to be one of the most robust and effective methods for reducing the influences of noise[18]. Thus, the following equation is employed to measure the variation in fringe density for identification of resonant peaks:

$$F=\sum_{x=1}^{M-1}\sum_{y=1}^{N-1} I(x,y)\times I(x+1,y)-\sum_{x=1}^{M-2}\sum_{y=1}^{N} I(x,y)\times I(x+2,y) \tag{14}$$

where $I(x, y)$ is the intensity of the interferogram image; and $M, N$ is the image pixel size of the window.

Influenced by the excitation frequency and the pulsed light duration, the intensity of the strobed light fluctuates during the scanning process. Accuracy of resonant modes detected will be undermined because the fringe contrast cannot be measured under a constant lighting situation. To address the issue, a more robust detection index, which evaluates a differential fringe density measure between neighboring scanning frequencies, is employed and can be expressed as follows:

$$\Delta F=(F_{f_1}-F_{f_2})^2 \tag{15}$$

where $F_{f_1}$ is the value of the fringe density measure when the vibration excitation frequency is $f_1$; $F_{f_2}$ is the value of the fringe density measure when the vibration excitation frequency is $f_1+\Delta f$; and $\Delta f$ is the scanning frequency pitch.

When the differential fringe density measure for all tested frequencies are determined, peak detection is then employed to search for all the peaks along the tested frequency axis. Finally, all possible resonant peaks detected are evaluated to verify the vibration modes.

## 5 Measurement examples and analyses

### 5.1 Theoretical simulation of beam dynamic analysis using ANSYS

A micro cantilever beam and a cross-bridge microbeam were employed for testing the developed resonant mode detection method. The microbeam was fabricated by NANOSENSORS Corp. and its detailed material specifications are shown in Table 1. Here, the material density, modulus of rigidity, Young's modulus and yield strength of silicon were set to be 2330 kg/m$^3$, $0.5\times10^{11}$ N/m$^2$, $1.69\times10^{11}$ N/m$^2$ (in the <110> direction) and $7\times10^9$ N/m$^2$ respectively. Figure 15 is a schematic diagram of the cross-bridge microbeam with its dimensional specifications. Simulation of this microbeam was performed using Equation (12) but with a different boundary condition.

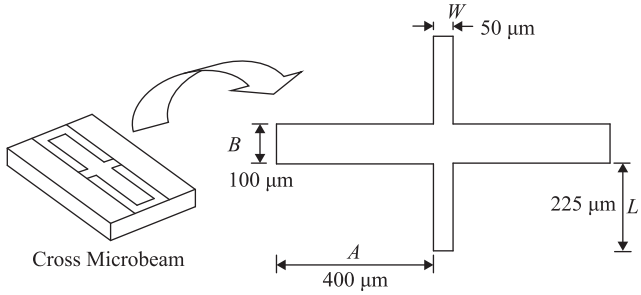


$A$, $B$, $L$, $W$= length of cross microbeam
$T$ = thickness (8 μm)
$\rho$ = density of silicon(2330 kg/m$^3$)
$E$ = modulus of elasticity/Young's modulus($1.65\times10^{11}$ N/m$^2$)
$v$ = Poisson Ratio(0.216)

Figure 15　Schematic diagram and the dimension specification of cross microbeam

A theoretical simulation for identification of the vibration modes of the AFM microbeam was performed using ANSYS. Figure 16 shows the first six mode values

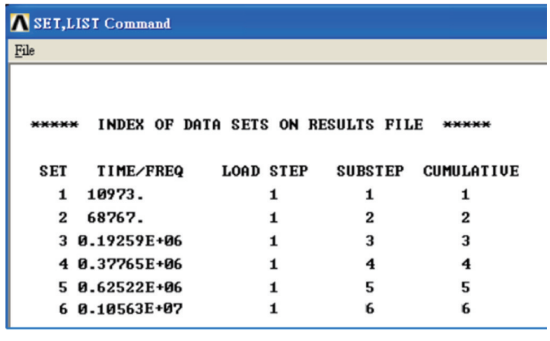
SET,LIST Command

File

***** INDEX OF DATA SETS ON RESULTS FILE *****

| SET | TIME/FREQ | LOAD STEP | SUBSTEP | CUMULATIVE |
|---|---|---|---|---|
| 1 | 10973. | 1 | 1 | 1 |
| 2 | 68767. | 1 | 2 | 2 |
| 3 | 0.19259E+06 | 1 | 3 | 3 |
| 4 | 0.37765E+06 | 1 | 4 | 4 |
| 5 | 0.62522E+06 | 1 | 5 | 5 |
| 6 | 0.10563E+07 | 1 | 6 | 6 |

Figure 16　ANSYS simulation results for the resonant vibration mode detection on a contact-modeAFM cantilever microbeam

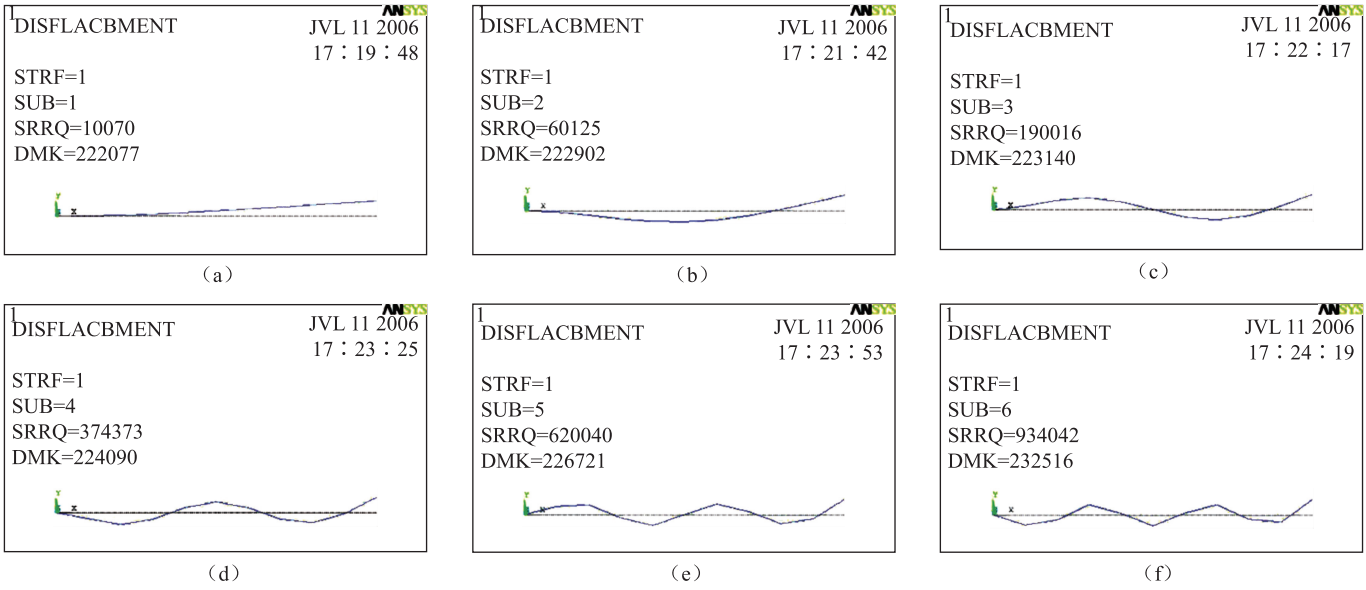


Figure 17 The theoretical simulation results of the AFM micro cantilever for the first six mode

simulated, whose natural frequencies predicted were 10.97, 68.77, 192.59, 377.65, 625.22 and 1056.30 kHz respectively. Figure 17 displays the theoretical simulation results of the AFM microcantilever for the first six modes. Figure 18 shows the first third modes of cross-bridge microbeam simulated, whose natural frequencies predicted were 31.49, 52.50 and 152.30 kHz respectively. The theoretical simulation results of the cross-bridge microbeam for the first three modes are shown in Figure 19.

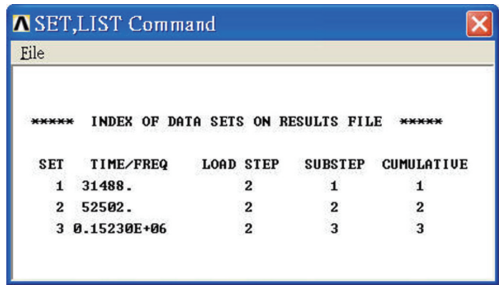


Figure 18 ANSYS results of the resonant vibration mode detection on the cross-bridge microbeam

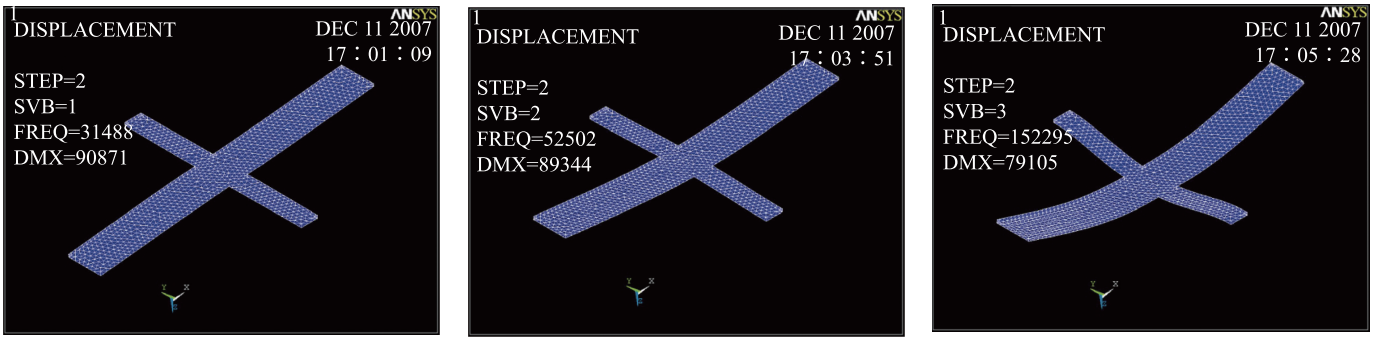


(a) The first mode (b) The second mode (c) The third mode

Figure 19 The theoretical simulation results of the cross-bridge microbeam for the first three resonant modes

## 5.2 Analysis results of automatic resonant mode detection

To detect and reconstruct out-of-plane mode shapes, the MEMS samples are actuated by applying a sinusoidal voltage generated by a 20 MHz function waveform generator. The two driving signals mentioned above are accurately synchronized with an adjustable phase delay in order to generate frozen interferograms. Meanwhile, the timing for CCD acquisition is synchronized with the stroboscopic lighting signal when the signal frequency is reduced to an adequate level for a common CCD frame rate, such as 30 frames per seconds. The whole measurement system is mounted on a vibration isolation

optical table and placed in an environment with minimum influence of external vibrations and air disturbances.

For the dynamic vibratory 3-D profilometry and automatic resonant mode detection, the tested devices are rigidly secured on a silicon holder (Point probe sensor). The holder is mechanically fixed onto a piezoelectric $Pb_x ZrTiO3_{l\_x}$ (PZT) disk, which is integrated with silver electrodes. Similarly, the vibration shaker and the cross-bridge microbeam were integrated with a piezoelectric cylinder driven by silver electrodes.

Figure 20 shows the differential fringe density measures for the AFM micro cantilever. These measurements were obtained using the developed vibratory mode detection method, in which the scanning range was set to be 1 ~ 1200 kHz and the scanning resolution was fixed at 0.1 kHz. By using peak detection in the developed method, the actual resonant mode frequencies measured and identified were 10.9, 63.9, 205.4, 403.1, 659.4 and 1001.3 kHz for the first six modes, respectively. As for the cross-bridge microbeam, the actual resonant mode frequencies measured and identified were 29.8, 55.8 and 159.2 kHz for the first three modes, respectively, as shown in Figure 21. The difference between the simulated resonant modes and the detected ones were within 7% of the resonant frequency, indicating that the developed resonant mode detection method is effective in finding the resonant frequencies of microstructures. Meanwhile, it is worth noting that some unexpected parasitic resonances may appear in the tested results but they can be filtered out by considering only the significant peaks in microbeam vibratory mode investigation.

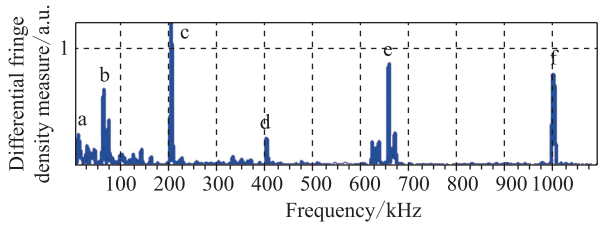


Figure 20　The differential fringe density measures being obtained on the tested contact-mode AFM microbeam using the developed detection method, in which the scanning range was set from 1 to 1200 kHz and the scanning resolution as 0.1 kHz (a to f represent the first six modes, respectively, being identified as the major vibratory ones)

Tables 2 and 3 detail the experimental results and the deviation between the theoretical and measured values for the AFM micro cantilever and the cross-bridge microbeam, respectively. Imperfection of simulations and material specifications may have accounted for the deviation. Furthermore, measurements of the tested microbeams were also made using a calibrated laser Doppler interferometer to verify the accuracy of the developed detection method. The first six modes of the contact-mode AFM cantilever were accurately identified by the interferometer as 10.8, 64.6, 200.9, 396.0, 649.2 and 1010.2 kHz, respectively; while the first

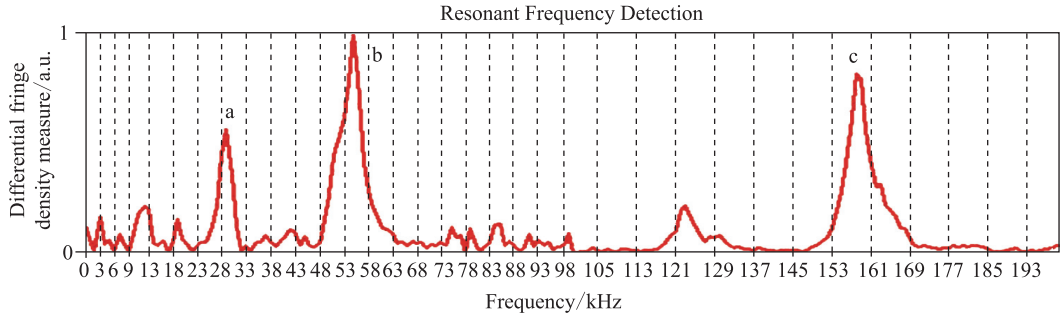


Figure 21　The differential fringe density measures being obtained on the cross-bridge microbeam using the developed detection method, in which the scanning range was set from 1 to 200 kHz and the scanning resolution as 0.1 kHz (a to c represent the first three modes, respectively, being identified as the major vibratory modes)

three vibratory modes of the cross-bridge microbeam were also identified as 28.9, 54.6, and 162.5 kHz, respectively. As can be seen, the predicted values were consistent with the experimental ones, and the difference between the predicted and experimental values obtained increased slightly when the vibratory mode was increased from one to six. Our experimental results confirmed that the measured values were in close agreement with the reference values obtained

from the interferometer, with the maximum deviation below 1.3 %.

Table 2 Experimental results from the automatic resonant mode detection on a contact-mode AFM cantilever microbeam

| Vibratory Mode | ANSYS Value /kHz | Measured Value /kHz | Difference /% |
|---|---|---|---|
| First Mode | 10.97 | 10.9 | -0.6 |
| Second Mode | 68.77 | 63.9 | -7.1 |
| Third Mode | 192.59 | 205.4 | 6.7 |
| Fourth Mode | 377.65 | 403.1 | 6.7 |
| Fifth Mode | 625.22 | 659.4 | 5.5 |
| Sixth Mode | 1056.37 | 1001.3 | -5.2 |

Table 3 Experimental results from the automatic resonant mode detection on the cross microbeam

| Vibratory Mode | ANSYS Value /kHz | Measured Value /kHz | Difference /% |
|---|---|---|---|
| First Mode | 31.49 | 29.8 | -5.4 |
| Second Mode | 52.50 | 55.8 | 6.3 |
| Third Mode | 152.30 | 159.2 | 4.5 |

### 5.3 Results and analysis of out-plane profilometry

A series of vibratory shapes at resonance modes were obtained using the white-light stroboscopic interferometry method developed. The mode shapes and cross-section contours were obtained by profiling the vertical scanning contours along the microbeam length. The AFM cantilever and cross-bridge microbeams were measured to reconstruct its static and dynamic surface profiles.

A 20-$V_{pp}$ sinusoidal voltage with different vibration mode frequencies was applied to the PZT driver and a 2% duty cycle of the strobed light was used for the stroboscopic measurements. Stroboscopic measurements with white-light vertical scanning interferometry of the vibration modes were performed at the first six frequency modes. To evaluate the initial beam status, the static 3-D surface profile was obtained using the developed white-light interferometric scanning method. Figure 22 shows the static surface profiles of the AFM cantilever beam. The 3-D maps illustrated in Figure 23 (a)-(i), represent sequentially the dynamic measurements for a successive series of delay phases. The maximum vibration amplitude was with in 400 nm. It should be noted that a small portion of the surface section was not detected. This was mainly due to the surface curvature of the measured contour section being larger than the maximum detectable range of the interferometric objective. Meanwhile, the static surface profiles and dynamic 3-D vibratory modes of the cross-bridge microbeam are shown in Figs. 24 and 25, respectively. As can be seen, the maximum amplitude of the vibratory mode was within 1200 nm, where the detected modes were consistent with the simulated ones.

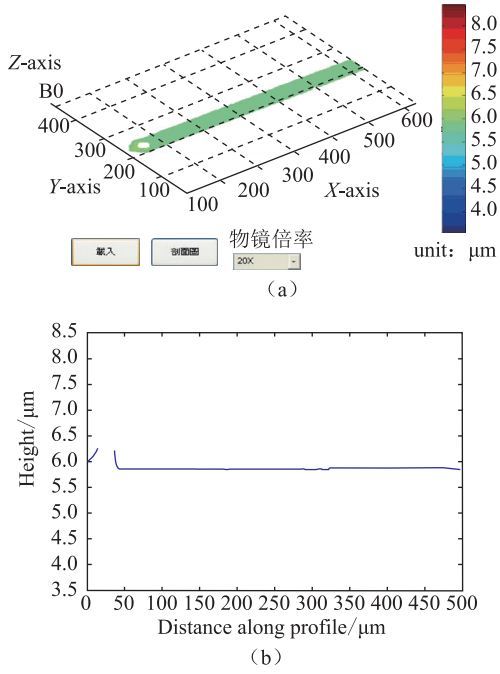


Figure 22 3-D map and cross section contour of the contact-mode AFM cantilever microbeam at its static mode

The experimental results have clearly demonstrated the capability of the developed optical system and white-light stroboscopic interferometry for dynamic profile measurement of complex vibratory behaviors operated in high frequency. Comparison between the simulation results shown in Figs. 17 and 19 reveals that the vibratory shapes and amplitudes were in close agreement with the ANSYS results. Nevertheless, slight inconsistency between the theoretical values and the measured ones was noticed, which may be due to the following.

1) Deviation in dimensions and material properties of the cantilever. Potential measurement errors and simplification of the theoretical analysis may result in errors of approximately 10% in the cantilever analysis.

2) Ends of the cantilever beam inadequately clamped. Tests on the cantilever beam are performed assuming

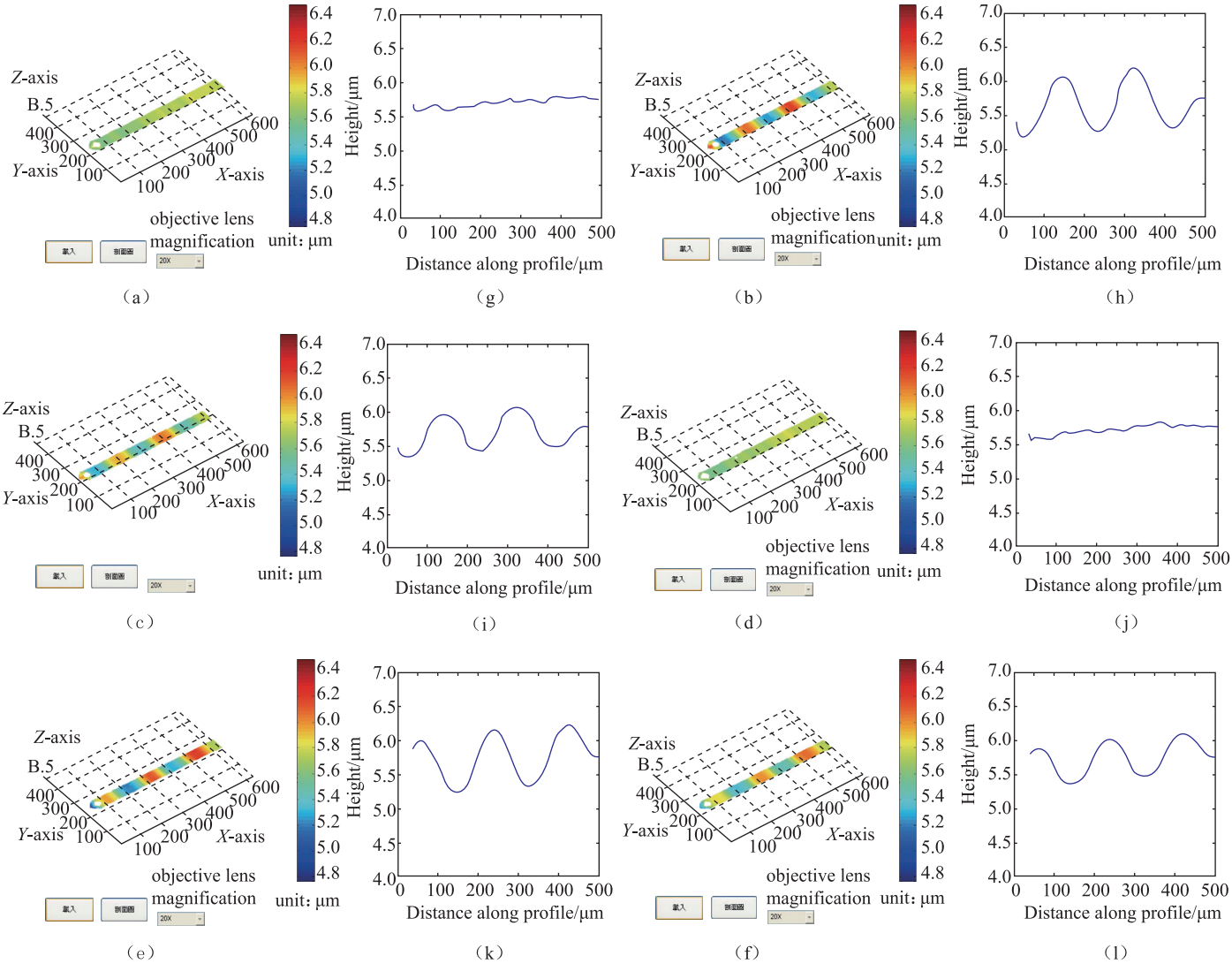


Figure 23　3-D map and cross section map of the sixth resonance modes: ((a) ~ (f)) representing mode shape and ((g) ~ (l)) representing the cross section contours at 0°, 60°, 120°, 180°, 240° and 300°, respectively

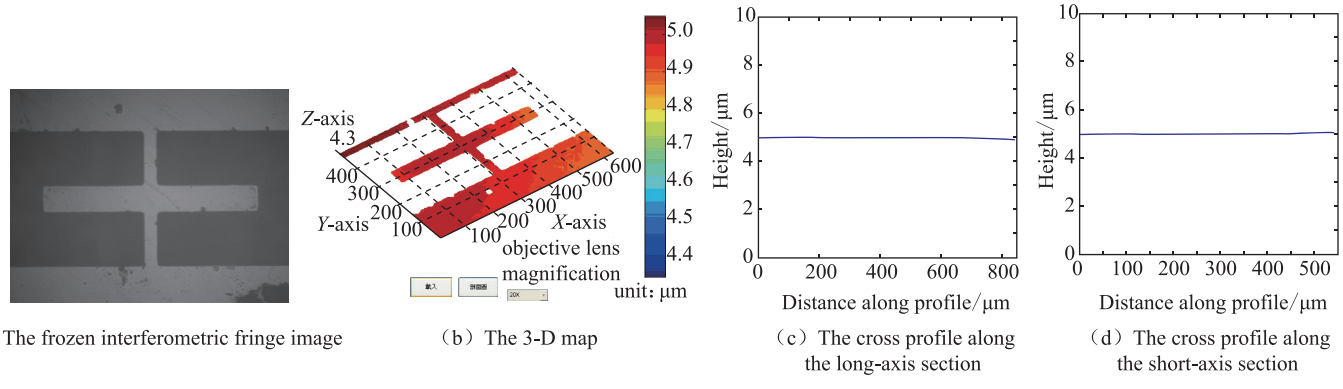


(a) The frozen interferometric fringe image　(b) The 3-D map　(c) The cross profile along the long-axis section　(d) The cross profile along the short-axis section

Figure 24　The 3-D map and cross section map of the tested cross-bridge microbeam at its static situation

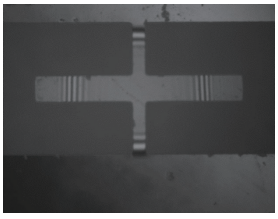

（a）The frozen interferometric fringe

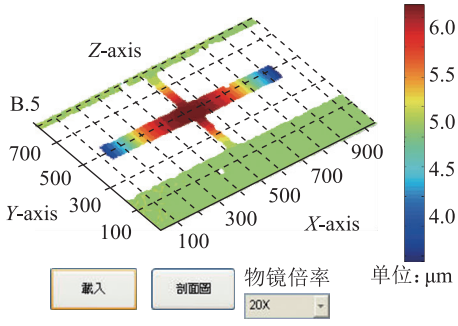


（b）3-D vibratory mode maps at 0°

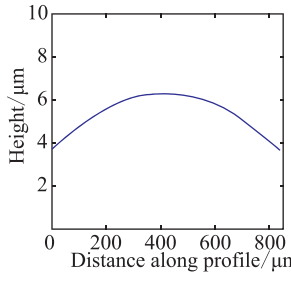


（c）The cross profiles of the long-axis section at 0°

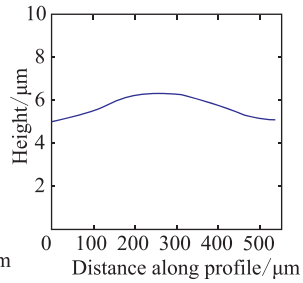


（d）The cross profiles of the short-axis section at 0°

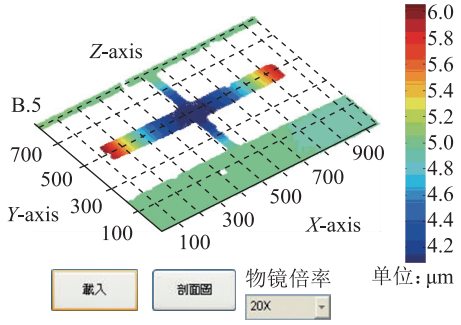


（e）3-D vibratory mode maps at 90°

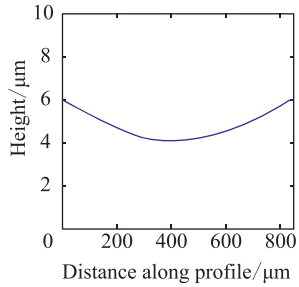


（f）The cross profiles of the long-axis section at 90°

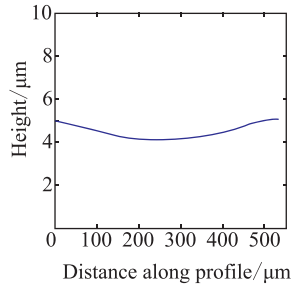


（g）The cross profiles of the short-axis section at 90°

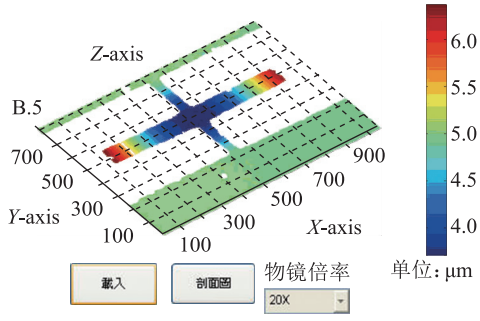


（h）3-D vibratory mode maps at 180°

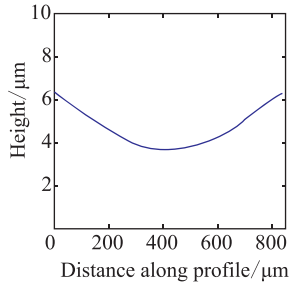


（i）The cross profiles of the long-axis section at 180°

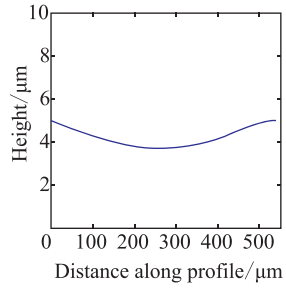


（j）The cross profiles of the long-axis section at 180°

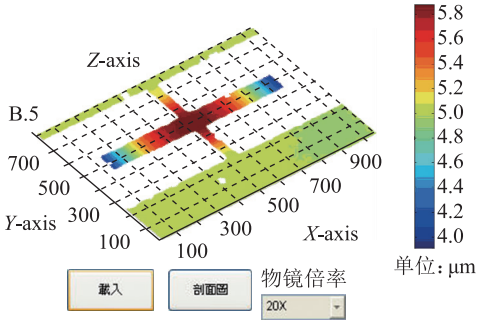


（k）3-D vibratory mode maps at 270°

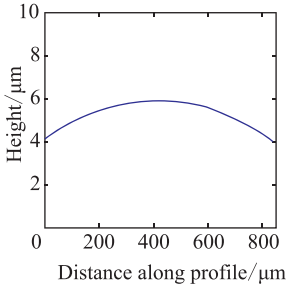


（l）The cross profiles of the long-axis section at 270°

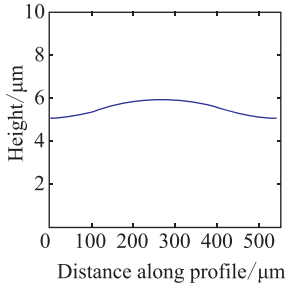


（m）The cross profiles of the long-axis section at 127°

Figure 25 The 3-D map and cross section map of the tested cross-bridge microbeam at its third resonance mode ($f$ = 159. 2 Hz)

that the end of the beam is perfectly clamped to its support base. Inadequate clamping may lead to deviations in results.

3) Distortion effect related to excessive pulsed lightenergy projected onto the cantilever microbeam. Potential distortion caused by excessive pulsed light energy may also contribute to differences between the simulated and experimental results.

Compared with other conventional methods for automatic

resonant frequency detection, the developed system does not require additional hardware. In other words, the developed method can perform automatic resonant frequency detection by employing a common stroboscopic optical system for out-of-plane vibratory mode measurement without the need to add any optical components or devices.

## 6 Non-conventional SWLI for self-exciting vibrating objects[13]

This session presents an approach for automatic resonant mode detection of microstructures using the non-conventional stroboscopic interferometry[13]. The conventional stroboscopic interferometry normally achieves the dynamic measurement by attaching a driving excitation source onto a tested sample and the same time connecting a synchronization device to its light source for synchronizing the frequency of the light source. However, many of the testing objects having an individual vibrating excitation source cannot be analyzed directly by the above method. For example, for those wide-band driving source such as a micro cantilever submerged in water which is resonated with the excitation of the flowing water, the traditional method is no longer suitable for dynamic measurement since it is difficult to control the resonance of the driving source. Therefore, a new stroboscopic interferometer employing a novel frequency-scanning method is proposed to identify the resonant frequency and dynamic characteristics of a vibratory microstructure having unknown excitation frequency.

### 6.1 Design of measurement system

Figure 26 shows the schematic diagram with the optical system developed for identifying dynamic characteristics of a vibratory microstructure. The details about Mirau stroboscopic interferometric system setup have been described in the previous works. The synchronization unit is employed to produce a fundamental signal for correspondingly generating a first and second synchronized signal in a manner that these two are synchronized with the fundamental signal. The synchronization unit is composed of a wave generator and a synchronization controller, in which the wave generator is able to respond to a request of the control center. The light-emitting unit, being coupled to the synchronization unit, is configured to receive the first sync. signal so as to generate a strobed light accordingly. The

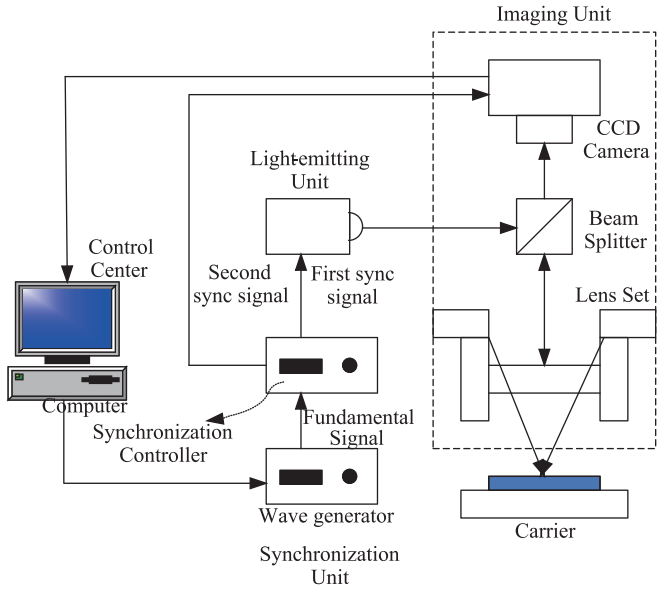


Figure 26　Schematic diagram of the system setup

imaging unit, also being coupled to the synchronization unit, is configured to receive the second sync. signal for controlling the imaging unit to capture an image of the vibratory microstructure while transmitting the captured image to the control center. The fundamental and second synchronized signals are accurately synchronized with an adjustable phase delay, in order to generate frozen interferograms. The significant difference between the conventional and non-conventional stroboscopic interferometry is the fact that the testing sample as described here is self-driven by its own excitation source with a unknown vibrating frequency for its resonance.

In the system, a light emitting diode or other light sources of equivalent capability can be applied as the light source. The repeatability of the LED firing timing was identified to be within 2.1 nanoseconds for ± one standard deviation. A strobed laser light is capable of producing a short light pulse with a frequency up to 10 MHz or higher while the LED light can generate a pulsed light with a pulsed period of 50 ~ 100 nanoseconds. Apparently, the laser diode flashes faster and provides a higher measurement bandwidth than the LED. However, the stroboscopic measurement based on LED is capable of characterizing dynamic behavior of MEMS up to several MHzs, which meets the general demands of dynamic characterization of modern MEMS systems. Furthermore, in reconstructing 3-D profile of object surface, the coherent length of white light LED source is

much shorter than that of laser light source. The white-light interferometry employed is capable of producing high quality of interferograms for evaluating dynamic surface vibratory modes.

To achieve accurate synchronization between the lighting and imaging unit, a fundamental (sinusoidal) signal is employed as a triggering source for generating the synchronizing signals in Figure 27. As soon as the synchronization controller receives the fundamental signal generated from the wave generator, a divider circuit in the synchronization controller produces a divider signal which is further converted to a square wave signal in the square-wave generating circuit. The signal is then delayed by the delay circuit to form a delay signal, so that the delay signal and the square wave signal are processed to form the first sync. signal for synchronizing the light-emitting unit. Meanwhile, the second sync. signal shown in Figure 28 can be also generated by either the delay circuit or the square-wave generating circuit for synchronizing the imaging unit.

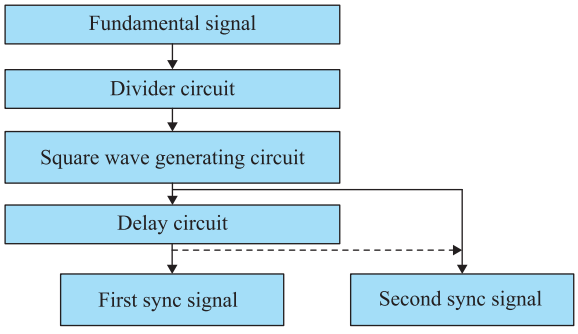


Figure 27 Signal processing flow chart of the synchronization controller

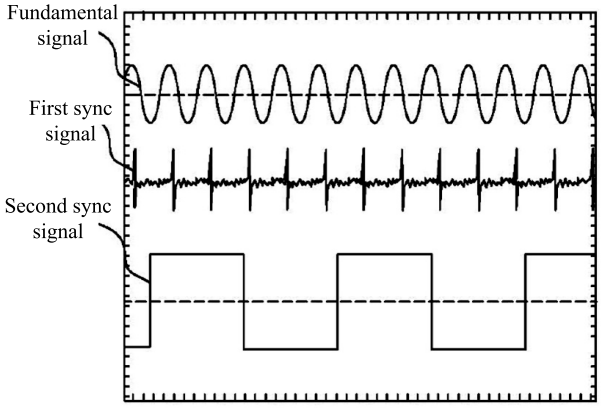


Figure 28 Illustration of the synchronized signals generated for system synchronization

### 6.2 Automatic resonant mode detection for self-vibrating microstructures usinginterferogram image

The proposed method is based on one of the distinct properties generally possessed in theinterferograms. By observing an example of an AFM microcantilever beam initially leveling at a horizontal orientation and then vibrating at two different modes (a non-resonant frequency and a resonant mode shown in Figure 29 and Figure 30, respectively), it can be observed that the interferogram image acquired from a vibration frequency closer to its resonant mode generally contains more high frequency component in its spectrum domain. Meanwhile, the image focus of the interferogram image is increased when the vibration is scanned approaching to its resonant frequency and reaches at a peak as the vibratory frequency is set exactly on any of the resonant modes.

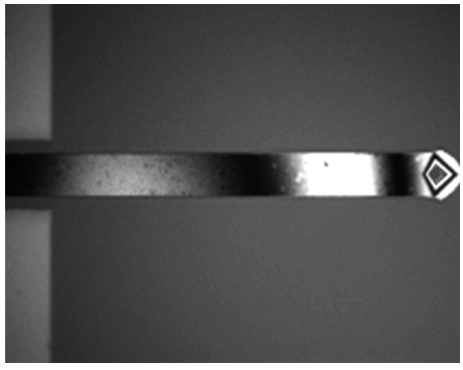

Figure 29 The white-light stroboscopic Interferogram image obtained from measuring an AFM contact-mode cantilever beam with a scanning frequency of 180.0 kHz, which was close but not exactly on its secondary resonant mode

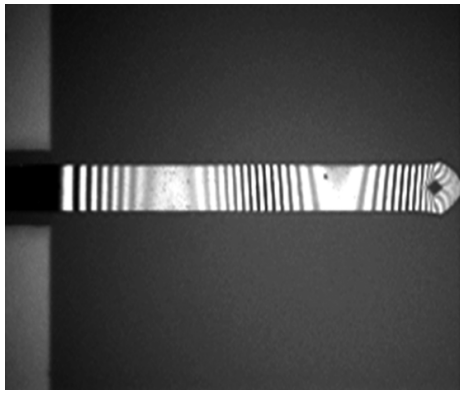

Figure 30 The white-light stroboscopic interferogram obtained from measuring an AFM contact-mode cantilever beam with a scanning frequency of 185.3 kHz, which was exactly on its secondary resonant mode

A scanning algorithm shown in Figure 31 is proposed to identify dynamic characteristics of a vibratory microstructure. The refereeing dynamic characteristic can be the periodic or non-periodic vibrating frequency of a vibratory microstructure, or its resonant frequency. At the beginning, a scanning frequency range and a frequency interval are adequately defined to meet with the measurement requirements. With these parameters, searching resonant frequency is performed by a selected frequency in the defined range until the working frequency is out of searching range. With the detected resonant frequencies, a 3-D surface profile can be obtained by full field stroboscopic interferometry.

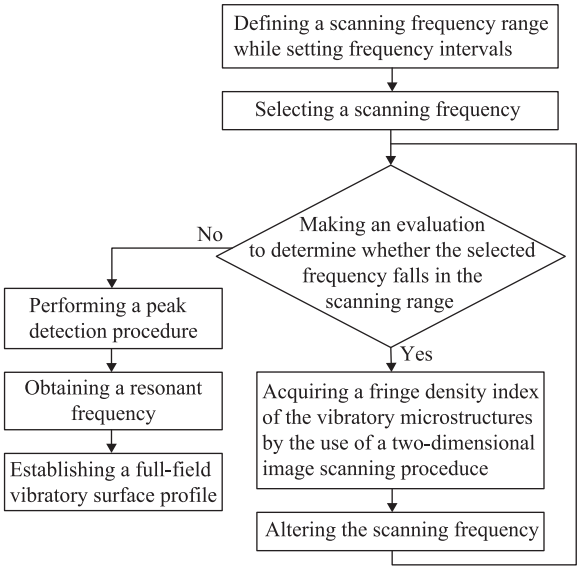


Figure 31　Flowchart of the proposed scanning algorithm for detecting the resonant frequency

### 6.3　Full-field stroboscopic interferometry

To obtain 3-D profile of object surface, a white light scanning interferometric irradiance is established along vertical position for every pixel. Example of a white light scanning interferometric irradiance is shown in Figure 32. The depth value z of measured pixel is calculated as the peak position of envelope signal.

For the automatic resonant mode detection and dynamic vibratory 3-D profilometry, the cross-bridge microbeam used in the previous session was rigidly secured on a silicon holder and vibrated at its resonant frequency (being pre-identified by a calibrated laser Doppler interferometer) by an

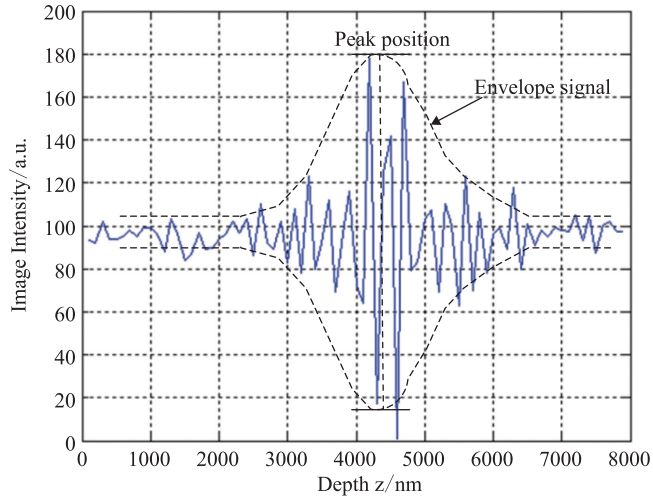


Figure 32　White light scanning interferometric irradiance captured by the designed interferometer

individual excitation source. Using ANSYS simulation, its first three natural frequencies were predicted as 31.49, 52.50 and 152.30 kHz, respectively. Using the developed resonant scanning method, the actual resonant mode frequencies of cross microbeam were measured and identified as 29.8, 55.8 and 159.1 kHz for the first three modes, respectively. Shown in Figure 33, the focus measures obtained by using the developed method, in which the scanning range was set from 1 to 200 kHz and the scanning resolution as 0.1 kHz. The differences between the simulated values and the measured ones were reasonably within 6.3%. The detailed results are shown in Table 4. Meanwhile, it is worth noting that some unexpected parasitic resonances and background noises may appear in the tested results but they can be filtered out by considering only the significant peaks in microbeam vibratory mode investigation. A general time averaging method can be also used to minimize the background noises.

More importantly, it was also identified that the measured results are consistent with the calibrated ones obtained from the Doppler interferometer. The detecting resolution of the proposed method is mainly determined by the scanning pitch. From Table 4, it clearly shows that the resonant modes detected both by the laser Doppler and the non-traditional stroboscopic methods were also almost identical. This indicates that the non-traditional stroboscopic method developed in the article is promising.

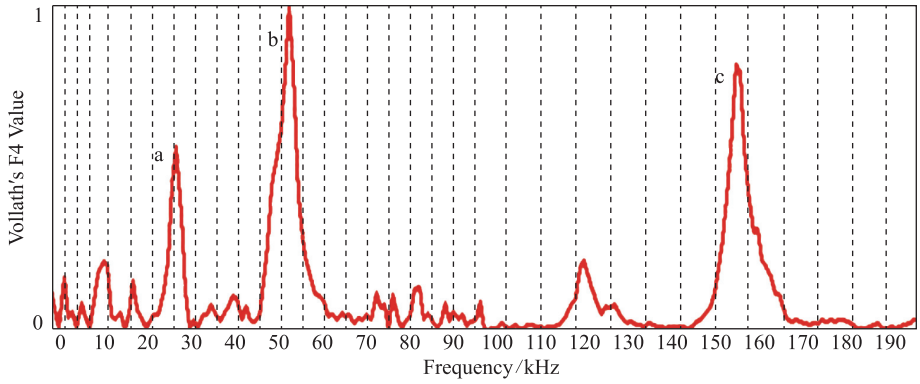


Figure 33 The focus measures obtained from measuring the cross-bridge microbeam using the developed detection method, in which the scanning range was set from 1 to 200 kHz and the scanning resolution as 0.1 kHz (a to c represent for the first three modes, respectively)

Table 1 Experimental results from the automatic resonant mode detection on thecross microbeam

| Vibratory Mode | Measured Value A /kHz | ANSYS Value B /kHz | Difference between A and B/% | Laser Doppler Value C /kHz | Difference between A and C/% |
|---|---|---|---|---|---|
| First | 29.8 | 31.49 | -5.4 | 29.9 | -0.33 |
| Second | 55.8 | 52.50 | 6.3 | 55.52 | 0.51 |
| Third | 159.1 | 152.30 | 4.46 | 158.06 | 0.66 |

In addition, to demonstrate its capability in obtaining the 3-D vibratory mode of the tested microbeam, the developed stroboscopic surface profilometer was employed to generate the dynamic 3-D profile measurement results at third resonant modes at 0° and 180° phase differences (shown in Figure 34). The results clearly indicate that the full-field 3-D vibratory mode of the microstructure can be fully characterized when the vibration excitation source was independently applied to the tested sample.

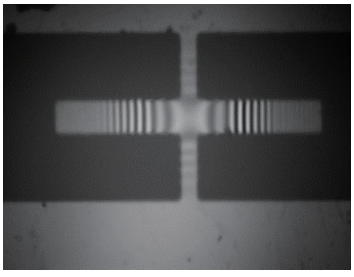

(a) The frozen interferometric fringe at 0° phase difference

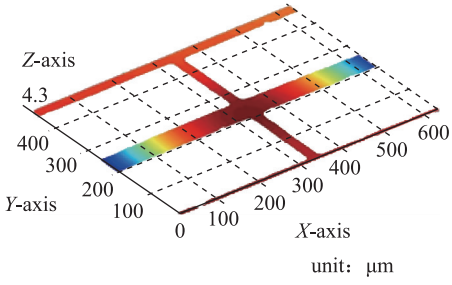


(b) The 3-D vibratory profile at 0° phase difference

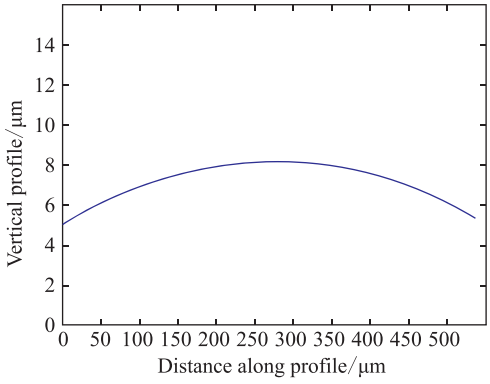


(c) The cross profile section of the mode at 0° phase difference

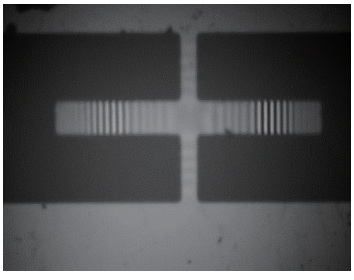

(d) The frozen interferometric fringe at 180° phase difference

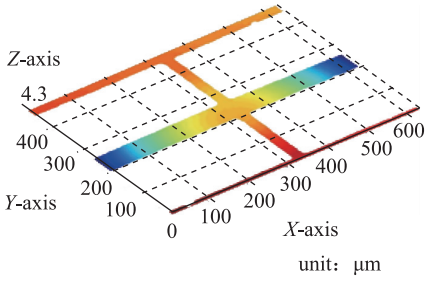


(e) The 3-D vibratory profile at 180° phase difference

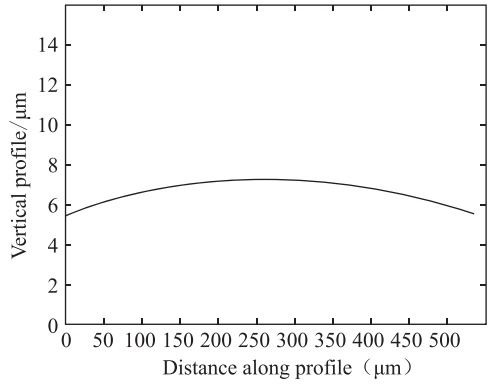


(f) The cross profile section of the mode at 180° phase difference

Figure 34 The dynamic 3-D profile measurement results of the tested cross microbeam at the third (159.1 kHz) resonance mode

## 7 Multi-functionoptical characterization and inspection[11,20]

In Micro-Electro-Mechanical-Systems (MEMS), mechanical elements, sensors, actuators, and electronics are integrated by using VLSI processing techniques[19]. The mechanical and chemical processes during MEMS fabrication affect the final shape and characteristics of the MEMS. Undesired defects can substantially affect the performance of the MEMS during its operation in dynamic modes, in which vibration is either in an in-plane or an out-of-plane. Thus, static and dynamic characteristics of MEMS must be accurately measured during inspection. Static characteristics, which include dimensions and surface topography, can be measured by common Phase-Shifting Interferometry (PSI) or by coherence scanning interferometry (CSI) systems.

Dynamic characteristics of MEMS can be categorized as either in-plane vibration or out-of-plane vibration. Many methods used to measure dynamic out-of-plane vibratory modes of micromechanical devices use single-beam laser Doppler vibrometers. However, these techniques are only effective for slow point-type scanning measurement and are very time consuming. Laser phase-shifting interferometry can also be combined with stroboscopic lighting to measure the surface of a vibrating MEMS. The surface measured or reconstructed in the study is referred as an areal surface due to a limited detection field of view in microscopic imaging. Digital holographic microscopy (DHM), which can be used to measure surface topography by using a holographic image, has also been applied in MEMS measurement by using a laser source and high speed camera for hologram acquisition. The technique enables measurement of mechanical behavior in MEMS. However, a drawback of the holographic microscopic is noisy fringe patterns caused by laser speckle phenomenon, which require further image processing techniques to reconstruct the surface topography. Another limitation of using single wavelength for measurement is that the measurable step-height detection range is limited by a quarter of wavelength. In all of the recent research development, the aim was to improve dynamic measurement accuracy without having to upgrade the current instruments.

To achieve multi-function optical characterization and inspection, the session introduces a stroboscopic coherence scanning Interferometry (SCSI) technique for measuring key characteristics typically used as criteria in MEMS inspections[19]. Surface profile of MEMS both static and dynamic condition is measured by means of or simply profiles of MEMS were obtained under both static and dynamic conditions by coherence scanning Interferometry (CSI). Resonant frequencies of vibrating MEMS were measured by deformation of interferogram fringes for out-of-plane vibration and by image correlation for in-plane vibration. The measurement bandwidth of the developed system can be tuned up to 3 megahertz or higher for both in-plane and out-of-plane measurement of MEMS[14]. This session introduces the techniques and strategies for performing static and dynamic measurements of MEMS by using SCSI. Although various techniques regarding SCSI for dynamic characterization of MEMS has been developed for many years, an SCSI optical testing platform has not been integrated with multi dynamic testing for MEMS characterization. Integrating these techniques enables the measurement of multiple MEMS characteristics with a single measurement platform. An integrated system is developed to measure characteristics such as surface topography in both static and dynamic conditions by means of phase shifting interferometry and CSI, resonant frequency detection by means of white light interferometry for out-of-plane vibrating samples and image correlation for in-plane vibrating samples. Repeatability and accuracy are evaluated by comparing the measurement results with reference instruments and by measuring standard samples.

### 7.1 Optical system design

Figure 35 illustrates the developed testing system, and Figs. 35(a) and (b) show the principle of the testing system and the developed platform, respectively. The system employs replaceable microscopic objectives for achieving different optical magnification with a tunable field of view (FOV). The microscope is equipped with a motorized X-Y stage and a nanometer-scale piezo electric transducer for performing vertical scans and phase shifting interferometric measurements. Figure 35(a) is schematic diagram of the developed optical system. The diagram shows that a Michelson or Mirau interferometric objective is used for full-

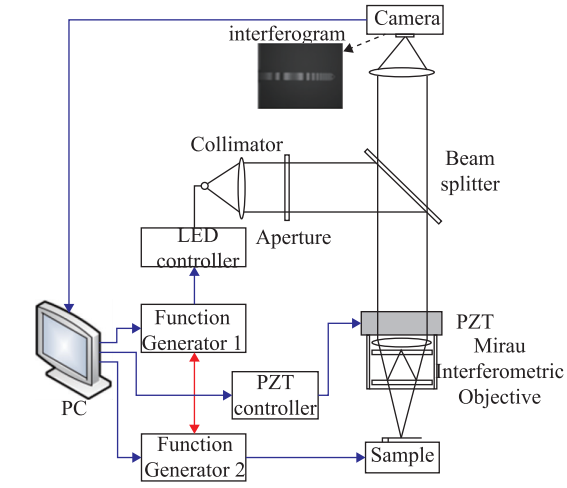


（a）Design of the testing system with stroboscopic lighting

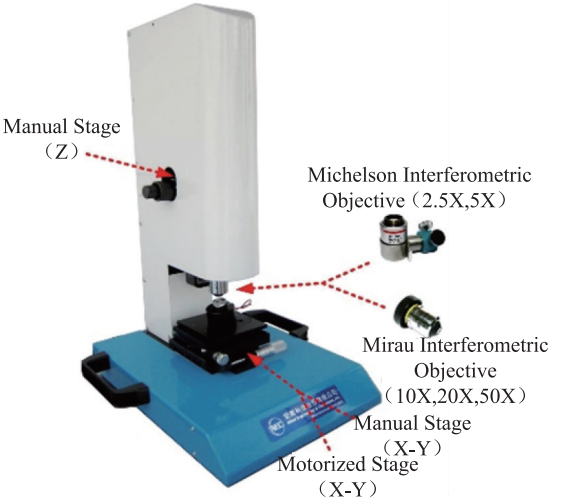


（b）Developed measurement platform by NTU

Figure 35 Developed SCSI system

field stroboscopic interferometry measurement. The optical system uses a set of optical lenses to collimate incident light from the light source module, which produces a parallel white light beam that illuminates the measured surface and the reference mirror. A single super luminescent light-emitting diode (SLED) is driven in pulse mode for stroboscopic dynamic measurement or is driven in continuous wave mode for static surface profilometry. Stroboscopic source illumination and signal synchronization are used to capture shifted periodic images during dynamic measurement of a vibrating sample. The synchronization system comprising a central control unit, a synchronous control unit, a vibration-driving unit, a light-emitting unit and an image-acquiring unit, is specifically designed for consistent motion-free image detection. Images can be acquired synchronously by coupling the image-acquiring unit to the central control unit. Signal synchronization is accurate to within several nano seconds. A driver in the lens module controls the interference objective when performing scanning interferometric measurements in surface profilometry. The beamsplitter receives the strobed light, guides it into a Mirau interferometric objective, and then projects it onto the vibrating sample.

For synchronization control, Figure 36(a) shows that the SLED pulsed light spectrum is generated and driven using a function generator while the function generator is synchronized with another function generator that produces an actuating sinusoidal signal for exciting the tested sample. Synchronizing these two function generators is essential for accurate measurement of either in-plane or out-of plane vibration. Figure 36(b) exhibits the sinusoidal signal for exciting the sample at the desired vibration and also shows the pulse signal used for stroboscopic lighting.

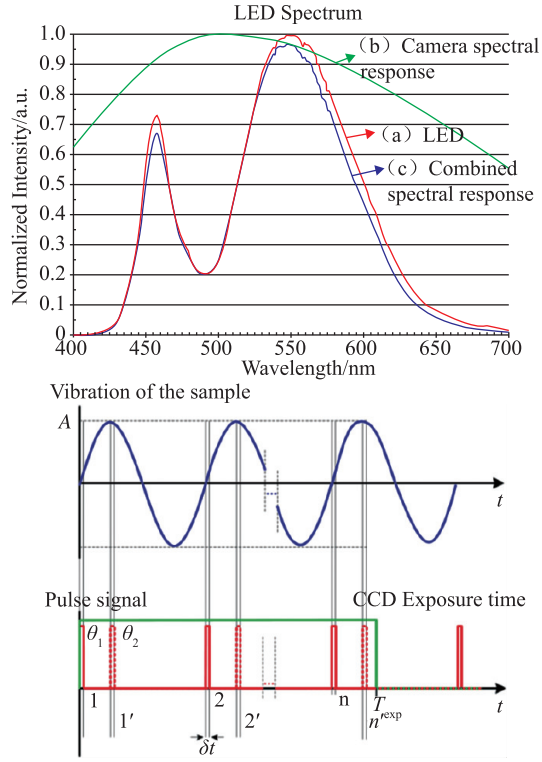


Figure 36 (a) Spectrum of the employed LED light source as measured by spectrometer; (b) synchronization signals between sinusoidal signal for vibrating sample and pulse signal for lighting

Shown in Figure 36(b), the phase delay between the sample vibration and the pulse signal ($\theta$) can be controlled to enable reconstruction of the vibration mode of the sample. The phase delay, $\theta_1$, is applied to perform reconstruction of the

object at 0° while the phase delay, $\theta_2$, is employed to perform reconstruction of the object at 90°. Using the similar principle, the complete vibration mode of the object can be reconstructed by applying different phase delays between the pulse light and vibration signal in one period of $2\pi$. Vibration mode reconstruction can be performed either for in-plane vibration or out-of-plane vibration. Accuracy of the measurement is mainly determined by two factors, namely synchronization of the function generators and duty cycle of the pulse signal. In the developed system, profile measurement is performed using CSI and PSI with an additional narrow band-pass filter to generate quasi-monochromatic light source. Static measurement accuracy is validated using standard calibration artifacts and varying step heights.

## 7.2 Measurement methodology

1) Static and dynamic profile measurement

In CSI measurements, the intensity of the interferometric fringe in an arbitrary region of the object under test can be expressed as

$$I(z) = I_0[1 + C(z - z_0)\cos(k(z - z_0) + \phi_0)] \quad (16)$$

where $I(z)$ is the interferometric light intensity that varies with position $z$ of the test surface; $I_o$ is the mean interferometric light intensity; $C(z - z_0)$ is the interference contrast; $k = \dfrac{2\pi}{\lambda}$ is the wave number of the light source; $z_0$ is the position of zero optical difference; and $\phi_0$ is the phase offset of the interferogram.

To measure a dynamic object vibrating at a certain frequency, Eq. (16) can be rewritten as

$$I(z(\omega,t,\Lambda)) = I_0[1 + C(z(\omega,t,\Lambda))\cos(k(z(\omega,t,\Lambda)) + \phi_0)] \quad (17)$$

where $z(\omega,t,\Lambda) = z_0 + \Lambda\sin(\omega t + \varphi)$ is the vibration displacement of the tested object as the function of time; $\Lambda$ is the amplitude of the vibration; and $\phi_0$ is the initial phase of the interferogram.

In SCSI, the light pulse can be modeled by a Gaussian function synchronized with the vibration signal as follows:

$$P(t) = P_c \cdot \mathrm{e}^{\frac{-(t-t_c)^2}{2\delta_t^2}} \quad (18)$$

where $\delta_t$ is the standard deviation in the stroboscopic pulse, $P_c$ is the maximum light intensity, and $t_c$ is the center of the stroboscopic pulse.

Intensity of the light pulse can be expressed as a function of the height of the tested object ($z$) as follows:

$$P(z(\omega,t,\Lambda)) = P_c \cdot \mathrm{e}^{\frac{-\left(\frac{1}{\nu}(z(\omega,t,\Lambda)-z_c)\right)^2}{2\delta_{z\tau}^2}} \quad (19)$$

where $z_c$ is the center position of the sample associated with the pulse center, $\delta_{z\tau}$ is the light intensity distribution along the $z$ axis, and $\nu$ is the vibrating speed of the object under test.

The interference light beam recorded by the camera, $I_s$, is modeled as the output of the convolution operation between the stroboscopic pulse $P(z(\omega,t))$ and the vibratory interferometric light intensity ($I$) of a vibratory object as follows[11]:

$$I_s(z(\omega,t,\Lambda)) = I(z(\omega,t,\Lambda)) * P(z(\omega,t)) \quad (20)$$

Therefore, the vibratory interferometric signal of SWLI can be modeled as

$$I_s(z(\omega,t,\Lambda),k) = \left[\int_{k_0}^{k_n} I_0[1 + C(z(\omega,t,\Lambda))\cos(k(z(\omega,t,\Lambda)) + \phi_0)]dk\right] * \left[P_c \mathrm{e}^{\frac{-\left(\frac{1}{\nu}(z_e+z_1(\omega,t)-z_c)\right)^2}{2\delta_{z\tau}^2}}\right] \quad (21)$$

The pulse length ($\delta t$) of the light beam can be considered by rewriting Eq. (6) as

$$I_s(z(\omega,t,\Lambda),k) = \int_{\theta_0}^{\theta_0+\delta t} I_s(z(\omega,t,\Lambda),k) * P(z(\omega,t))\,\mathrm{d}t$$

$$I_s(z(\omega,t,\Lambda),k) = \int_{\theta_0}^{\theta_0+dt} \left\{\left[\int_{k_0}^{k_n} I_0[1 + C(z(\omega,t,\Lambda))\cos(k(z(\omega,t,\Lambda)) + \phi_0)]\,\mathrm{d}k\right] * \left[P_c \mathrm{e}^{\frac{-\left(\frac{1}{\nu}(z_e+z_1(\omega,t)-z_c)\right)^2}{2\delta_{z\tau}^2}}\right]\right\}\mathrm{d}t \quad (22)$$

where $\theta_0$ is the initial time of the stroboscopic pulse corresponding to the phase delay of the pulse with respect to the sinusoidal vibration and $\delta t$ is the length of the stroboscopic pulse cycle time.

In PSI measurements, intensity of the interferometric fringe is calculated using an equation similar to Eq. (16) but with $C(z)$ assumed to be a constant within the depth of field of the interference objective. For the five-step PSI, five interferograms are captured with a 90° phase shift (equivalent to $\lambda_c/8$), and the object phase is calculated using the following five-step phase wrapping algorithm:

$$\phi = \arctan\frac{2(I_1 - I_3)}{2I_2 - I_4 - I_0} \quad (23)$$

where $\phi$ is the phase of the surface; $I_n$ is the intensity

of the interferogram at certain phase step ($n=0$ for 0°, $n=1$ for 90°($\pi/2$), $n=2$ for 180°($\pi$), $n=3$ for 270°($3\pi/2$), $n=4$ for 360°($2\pi$)).

The resulting wrapped phase is first converted from 0° ~ 180° into 0° ~ 360° range by performing Euler transformation. Phase unwrapping is then performed to reconstruct phase map of the test surface. Since the arctangent function produces results in the range $(-\pi/2, \pi/2]$ and the phase value is actually in $[0,2\pi)$, the Euler Equation is required to map the phase into $[0,2\pi)$.

Suppose

$$\phi = \arctan\left(\frac{\sin\phi}{\cos\phi}\right) = \arctan\left(\frac{\mathrm{Im}}{\mathrm{Re}}\right) \tag{24}$$

The Euler equation considers the signs of both real and imaginary components and places the angle in the correct quadrant[15]:

$$\phi(x,y) = \begin{cases} \phi(x,y) \text{ for } \mathrm{Im} \geqslant 0 \text{ and } \mathrm{Re} > 0 \\ \phi(x,y) + \pi \text{ for } \mathrm{Re} < 0 \\ \phi(x,y) + 2\pi \text{ for } \mathrm{Im} < 0 \text{ and } \mathrm{Re} < 0 \\ \dfrac{\pi}{2} \text{ for } \mathrm{Im} > 0 \text{ and } \mathrm{Re} = 0 \\ \dfrac{3\pi}{2} \text{ for } \mathrm{Im} < 0 \text{ and } \mathrm{Re} = 0 \end{cases} \tag{25}$$

Figure 37 shows an example of measurement results for a standard step height. Figure 38(a) shows the 3-D profile of the measured object, and Figure 38(b) shows a 2-D cross section of the profile. The nominal value of the step height is 24 nm (written as 0.024 μm on the sample) and the measured result for 30-time measurement is (24.2 ± 0.058) nm. A Mirau interferometric objective with 20X magnification was employed in this measurement.

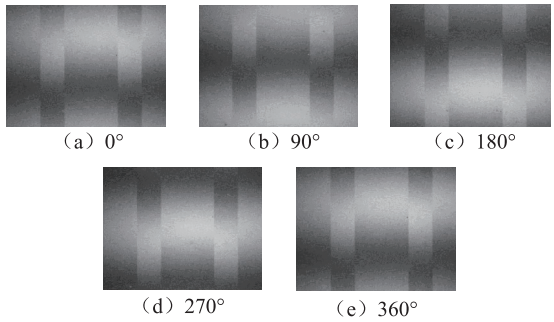


Figure 37 Interferograms for phase shifts in the following five steps

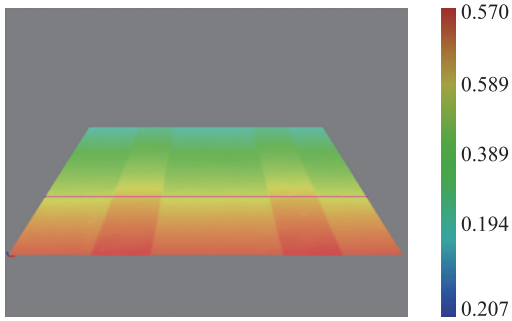


(a) 3D profile of a standard step height

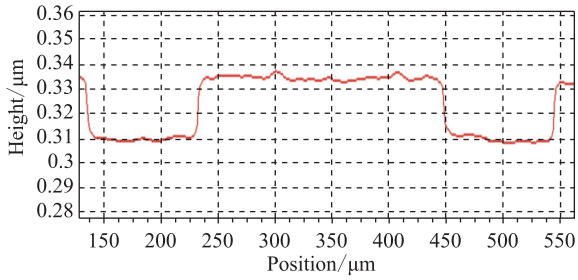


(b) The cross section of the measured sample

Figure 38 Measurement of a standard step height

The principle of using the developed SCSI system for dynamic surface profile measurement was comprehensively described in[11,15-16]. The CSI is used to reconstruct the

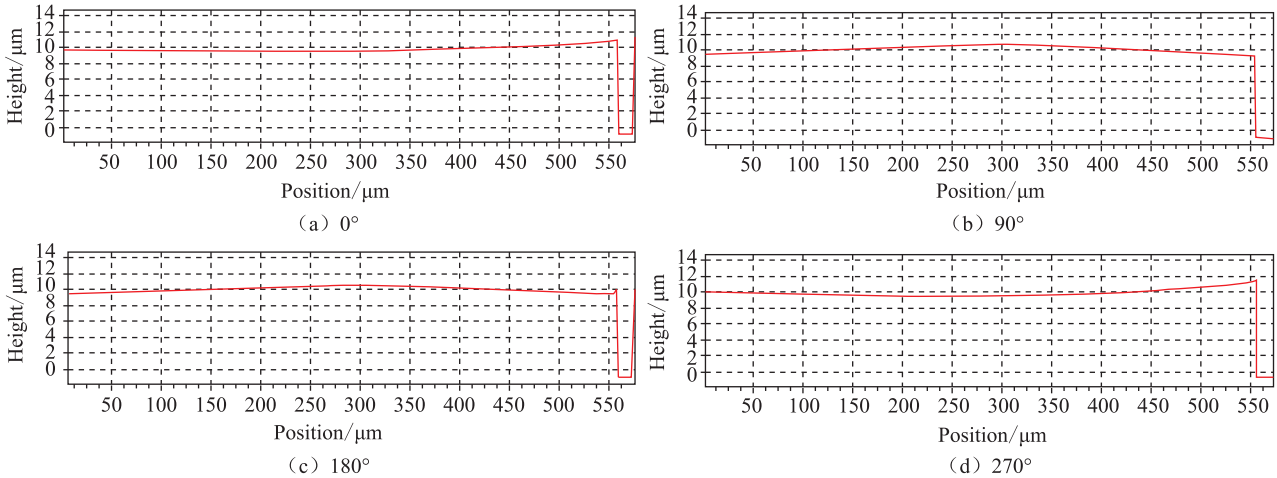


Figure 39 SCSI measurement results for AFM cantilever beam vibrating at 81.018 kHz at phase delay: (a) 0°; (b) 90°; (c) 180°; and, (d) 0°, respectively; and the 2D cross section at phase delay: (a) 0°; (b) 90°; (c) 180°; and, (d) 270°, respectively

surface profile of the vibrating object. In this study, an AFM cantilever was used to perform this test. The sample was vibrated at its first resonant frequency. The previous measurement in this system was 81.018 kHz. Figure 39(a-d) show 2-D cross section profiles of the AFM cantilever beam.

2) Resonant frequency detection for out-of-plane vibration

Resonant frequency in a mechanical system is the frequency that induces vibration to a maximum amplitude. In the white lightinterferometric system, this phenomenon is clearly observable and is automatically detected by the change in the interferogram pitch during vibration. The amplitude of the vibration changes the pitch of the interferogramic fringes, and the interferometric fringe pitch decreases as the vibration amplitude increases. This effect was demonstrated by an experiment in an AFM cantilever beam.

Figure 40 (a) shows the interferogram of the sample when the vibration frequency is not the resonant frequency. In contrast, Figure 40 (b) shows the interferogram of the sample when vibrated at its resonant frequency. The figures show that the pitch of the interferometric fringe is reduced to a minimal value when the sample is vibrating at its resonant frequency. This behavior enables accurate scanning and detection of the resonant frequency by recording and detecting the pitch of the interferometric fringe during the sample out-of-plane vibration.

(a) Non-resonant frequency　(b) Resonant frequency

Figure 40　Interferogram of the AFM cantilever vibrating at non-resonant frequency and resonant frequency

Based on the above principle, the resonant frequency is detectable by analyzing the spatial frequency of the interferogram at different scanning frequencies of the sample. The most effective method for analyzing the spatial frequency component of the interferogram is Fast Fourier Transform (FFT), which accurately extracts the frequency components and spectrum analysis.

The frequency scanning procedure is performed in a course scanning stage and in a fine scanning stage. With the coarse scanning result obtained ($f_{coarse}$), the fine scanning is then performed around $f_{coarse}$ with an adequate frequency scanning pitch when the scanning range is set from ($f_{coarse}-1$) to ($f_{coarse}+1$) kHz with a frequency scanning pitch of 0.1 kHz. In this range, the same spectrum analysis algorithm is used for the final frequency scan, and centroid detection method is used to calculate the fine peak. Figure 41 shows the density of the fringe as a function of frequency. As seen in Figure 41, a resonant frequency of 81 kHz was detected by the coarse scan and 81.018 kHz then detected from the fine scan. The repeated measurement had a standard deviation of 0.12 kHz. The resolution of resonant frequency detection can be increased by using a finer frequency scanning pitch.

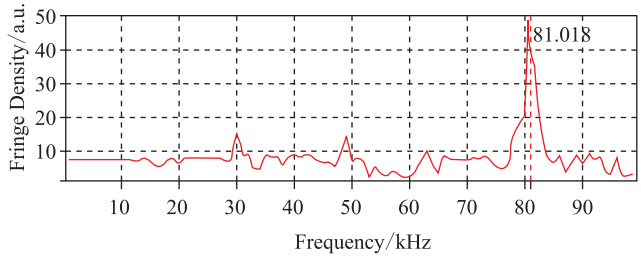


Figure 41　Results for out-of-plane resonant frequency measurement of the AFM cantilever beam

According to thedeconvolution algorithm developed in Ref.[11], the 7th mode resonant frequency of the cantilever beam in the tested AFM was 3.7334 MHz, which was consistent with the theoretical estimation. This indicates that the measurement bandwidth of the developed testing platform can reach several megahertz.

3) Resonant frequency detection for in-plane vibration

The developed system can use a similar scanning frequency detection principle to detect in-plane resonant frequency through the developed in-plane resonant frequency scanning process described in Figure 42. A region of interest (ROI) is first set at the vibrating region of the device. The change in motion is then tracked by capturing a series of images at different phases of vibration. The algorithm searches the resonant frequency in the wide range $[f_{start}, f_{end}]$ with the resolution of $f_{pitch}$ in the searching step. At each scanning frequency, motion vectors between images that have different vibration phases are identified, and a motion vector table is created to analyze the magnitude of difference in one cycle of vibration. The motion vectors are converted to actual displacement after using a standard resolution target (USAF 1951) to calibrate

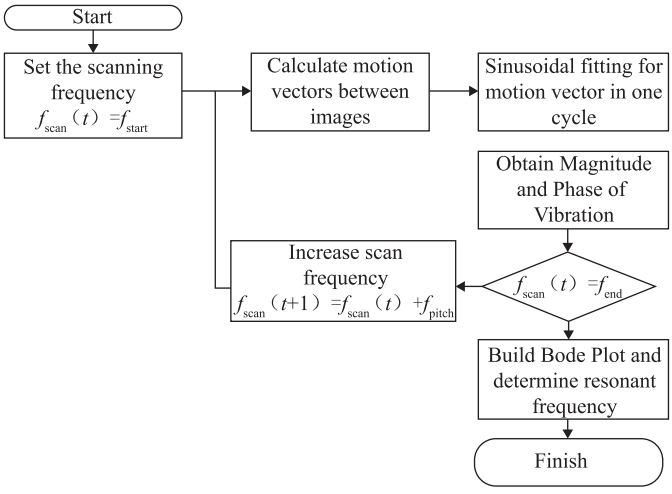


Figure 42 Flowchart of in-plane resonant frequency measurement process

the lateral resolution of the microscope. The lateral resolution of the developed system using 50X microscope objective is 0.140 μm/pixel.

The above detection process uses a sub-pixel template matching technique based on image correlation to increase accuracy in measuring motion vectors. The template must be matched at every possible orientation of the sample. A matching score based on normalized cross correlation is evaluated at each orientation and the highest matching score determines the motion vector. The formula of normalized cross correlation is calculated for each orientation, and the highest matching score determines the motion vector. The formula for the normalized cross correlation is

$$c=\frac{n\sum_{i,j}A_{ij}B_{ij}-\sum_{i,j}A_{ij}\sum_{i,j}B_{ij}}{\sqrt{n(\sum_{i,j}A_{ij}^2)-(\sum_{i,j}A_{ij})^2}\sqrt{n(\sum_{i,j}B_{ij}^2)-(\sum_{i,j}B_{ij})^2}} \quad (26)$$

where $c$ is cross correlation; $n$ is the number of pixels in the template or source image; $A_{ij}, B_{ij}$ are intensities of the template and source image at position $(i,j)$ of image coordinate, respectively.

When objects in the image are rotated with respect to each other, a set of templates at different orientations is employed for matching. The rotation invariant template matching method employs the fluctuating scope of the rotation angle which can be adequately defined in the template image. The search process compares all template patterns with a source image.

Notably, two methods can be used to improve the acquired image quality in the developed system. One is to increase the spatial resolution of the hardware setup. Theother option is to resample the image intensity to a higher spatial resolution through sub-pixel interpolation. Since the intensity interpolation approach is generally independent of image resolution, this method was applied in this study. The resolution of the original image can be increased by multiplying the image dimensions and their intensity values. After the multiplication process, a median filter is used to smooth the image while maintaining the continuity of image intensity. The motion vectors are calculated by conventional template matching for new images. The actual motion vectors of the original image can be obtained by dividing the motion vectors of the new images to the multiplied coefficient.

### 7.3 Measurement experiment and result analyses

The tested sample was an electrostatic comb drive with an actuator that enables comb structures to be moved simultaneously by applying a voltage and an excited frequency. In the measurement experiment, the resonant frequency of the comb drive and applied voltage were 2.7 kHz and 5 V, respectively. Figure 43 illustrate the image of the comb drive and its captured images from the developed SCSI system, respectively. Figure 43 (b) shows that the center of the drive is stationary. The two moving structures in the drive are indicated by the red ellipses.

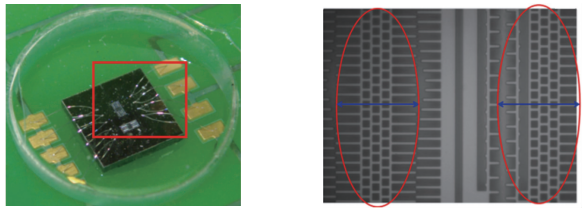

(a) Image of a MEMS comb drive (b) Vibrating parts of the comb drive captured by the microscopic system

Figure 43 In-plane measurement of a MEMS comb drive

Figure 44 shows the motion vector obtained by the developed cross correlation method, and Figure 44(a) shows the region of the MEMS where the motion vectors are detected. Figure 44(b) displays the resulting motion vectors.

Generally, a Bode plot can describe the characteristics of the vibration. A Bode plot includes a magnitude plot, which expresses the magnitude of the frequency response gain and phase plot, which expresses the frequency response phase shift. Figure 45 shows that a Bode plot is established by using a sinusoidal fitting technique to express the detected motion vectors as the magnitude and phase shift at each frequency.

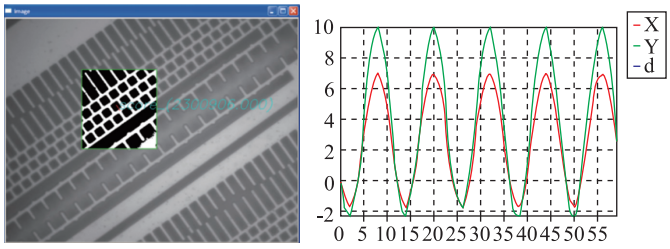


（a）The region of the comb drive used for motion vector calculation　（b）The calculated motion vector

Figure 44　Measurement result of a motion vector

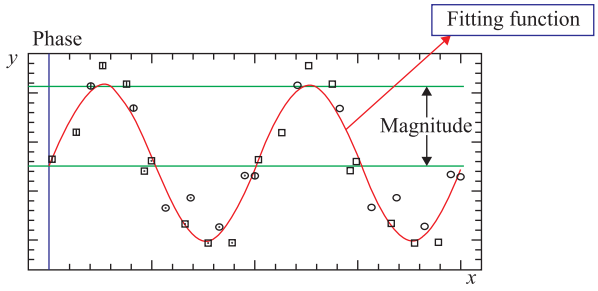


Figure 45　Sinusoidal fitting for calculating vibration magnitude and phase

After the Bode diagram is completed, the resonant frequency of in-plane motion can be further detected by finding the peak position in its magnitude diagram. In Figure 46, the magnitude *versus* frequency diagram clearly indicates the effect with the highest and sharpest peak, which is represented by the region where the resonant frequency occurs. The scan was performed at a range of 0.1 to 5 kHz and at a pitch of 0.05 kHz. The resonant frequency of the tested sample shown in Figure 46(a) was measured as 2.700 kHz. The repeated measurement result of resonant frequency is (2.692 ± 0.012) kHz.

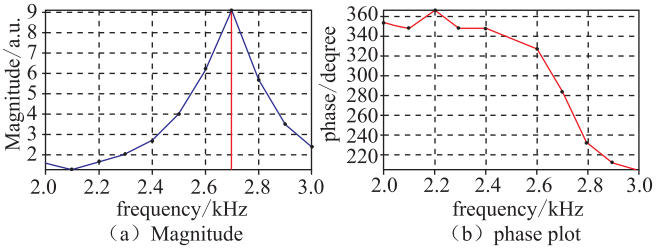


（a）Magnitude　（b）phase plot

Figure 46　Resonant frequency determination from magnitude and phase plot

A multi-function optical inspection methodology using SCSI is described here for identifying key characteristics of MEMS by both in-plane and out-of-plane measurement. Experiments showed that the developed methods are effective for 3D profile measurement in both static and dynamic samples. Meanwhile, a series of the resonant frequencies of the tested object can be precisely characterized for both of in-plane and out-of-plane vibration. The developed detecting principle and process enables accurate measurement of resonant frequency. The out-of-plane vibrating mode can be reconstructed by CSI with a vertical accuracy up to 10 nm and a detecting frequency can reach to several megahertz. The accuracy of the developed system was validated using standard samples. Full-field and high S/N measurement of CSI can be fully embedded with the developed method for profilometric characterization of MEMS in both static and dynamic modes. For these reasons, the SCSI method is superior to laser detection strategies.

## 8　Prospect of Technology

The development technology can be widely applied for high precision 2D, 3D and 4D surface static and dynamic measurement of microstructures, microsystems, MEMS and MOEMS. The measurable bandwidth of the developed method can be extended to several megahertz. This makes the method particularly useful for both static precise profilometry and dynamic characterization. White light interferometry (WLI) can provide high signal to noise ratio for high precision nano-scale 3D surface measurement in a full-field scale while SWLI can provide an excellent 4D (3D plus Time) dynamic structure characterization. In conclusion, the technology is essential to multi-dimension optical metrology and characterization of microsystems for system optimization and industrial realization.

### Acknowledgments

The author would like to convey his great appreciation to his previously supervised students and cooperating researchers for their contribution to this work in performing experimental tests, excellent discussions and brainstorming. The list of these contributors includes Dr. Abraham Mario Tapilouw, Dr. Calvin C. Chang, Mr. Yao – Tin Huang, Dr. Xuan Loc Nguyen, Mr. Jin – Liang Chen, and Mr. Huang – Win Lai.

### References

[1] Chen L C, Tapilouw A M. Theoretical simulation and experimental confirmation of duty cycle effect on stroboscopic white light interferometry for M(O)EMS dynamic characterization [J]. Journal of Micromechanics & Microengineering, 2013, 23(11):5008.

[2] Harris J S, Fusek R L, Marcheski J S. Stroboscopic interferometer

[J]. Applied Optics, 1979, 18(14): 2368.
[3] Montgomery P, Anstotz F, Montagna J. High-speed, on-line 4D microscopy using continuously scanning whitelight interferometry with a high-speed camera and real-time FPGAimage processing [C]// Optical Measurement Systems for Industrial Inspection VII. International Society for Optics and Photonics, 2011: 808210 – 808219.
[4] Andres M V, Tudor M J, Foulds K W H. Analysis of an interferometric optical fibre detection technique applied to silicon vibrating sensors [J]. Electronics Letters, 2007, 23(15): 774 – 775.
[5] Gutierrez A O, Edmans D M, Seidler G, et al. MEMS metrology station based on two interferometers[J]. Proceedings of SPIE-The International Society for Optical Engineering, 1997, 3225: 23 – 31.
[6] Speller K, Lawrence E M. Unique MEMS characterization solutions enabled by laser Doppler vibrometer measurements [J]. Proceedings of SPIE-The International Society for Optical Engineering, 2002, 4827: 478 – 485.
[7] Hunsinger J J, Serio B. FPGA Implementation of a Digital Sequential Phase-Shift Stroboscope for In-Plane Vibration Measurements With Subpixel Accuracy [J]. IEEE Transactions on Instrumentation & Measurement, 2008, 57(9): 2005 – 2011.
[8] Bosseboeuf A A, Gilles J P, Danaie K, et al. Versatile microscopic profilometer-vibrometer for static and dynamic characterization of micromechanical devices [J]. Proceedings of SPIE-The International Society for Optical Engineering, 1999, 3825: 123 – 133.
[9] De G P. Stroboscopic white-light interference microscopy [J]. Appl Opt, 2006, 45(23): 5840 – 5844.
[10] Petitgrand S, Bosseboeuf A. Simultaneous mapping of phase and amplitude of MEMS vibrations by microscopic interferometry with stroboscopic illumination[J]. Proc Spie, 2003, 5145: 33 – 44.
[11] Chen L C, Huang Y T, Nguyen X L, et al. Dynamic out-of-plane profilometry for nano-scale full-field characterization of MEMS using stroboscopic interferometry with novel signal deconvolution algorithm[J]. Optics & Lasers in Engineering, 2009, 47(2): 237 – 251.
[12] Chen L C, Huang Y T, Lai H W, et al. Innovative automatic resonant mode identification for nano-scale dynamic full-field characterization of MEMS using interferometric fringe analysis[J]. Measurement Science & Technology, 2008, 19(12): 125303.
[13] Chen L C, Nguyen X L, Huang H S, et al. Dynamic Surface Profilometry and Resonant-Mode Detection for Microstructure Characterization Using Nonconventional Stroboscopic Interferometry [J]. IEEE Transactions on Industrial Electronics, 2010, 57(3): 1120 – 1126.
[14] Chen L C, Huang Y T, Chang P B. High-Bandwidth Dynamic Full-Field Profilometry for Nano-Scale Characterization of MEMS[C]// JOURNAL OF PHYSICS, 2006: 1058 – 1062.
[15] Hirabayashi A, Ogawa H, Kitagawa K. Fast surface profiler by white-light interferometry by use of a new algorithm based on sampling theory[J]. Appl Opt, 2002, 41(23): 4876 – 4883.
[16] Hanhijärvi K, Aaltonen J, Kassamakov I, et al. Effect of LED spectral shift on vertical resolution in stroboscopic white light interferometry[C]// Proc. SPIE 7003, 2008: 70031S.
[17] Pavlicek P, Soubusta J. Measurement of the influence of dispersion on white-light interferometry [J]. Applied Optics, 2004, 43(4): 766 – 70.
[18] Santos A, Ortiz d S C, Vaquero J J, et al. Evaluation of autofocus functions in molecular cytogenetic analysis[J]. J Microscopy, 1997, 188(3): 264 – 272.
[19] Tapilouw A M, Chen L C, Loc N X, et al. Multi-function optical characterization and inspection of MEMS components using stroboscopic coherence scanning interferometry [J]. Advanced Optical Technologies (AOT), 2014, 3(4): 407 – 416.

## Author Introduction

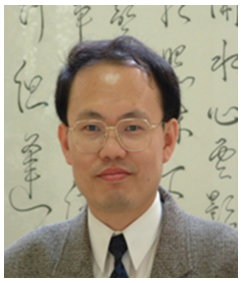

Prof. **Liang – Chia Chen** is currently working as a distinguished professor in the Department of Mechanical Engineering of National Taiwan University (NTU), Taiwan. He obtained his Ph. D. in advanced manufacturing and mechanical engineering, the University of South Australia in 2000. Prior to embarking on his academic career in Taiwan, he worked as a full – time research engineer in Gerard Industries of Australia (Clipsal) between 1996 – 2000 and Institute of nuclear energy research (INER) of Taiwan between 1991 – 1995. Before joining NTU, he worked as a distinguished professor in National Taipei University of Technology between 2001 – 2009 in Taipei. Up to now, he has received the outstanding research award from the Ministry of Science and Technology (MOST) of Taiwan in 2016, National year invention gold awards consecutively in 2013 & 2014, and the 2014 outstanding award on technology transfer from the MOST. His major research fields are in precision metrology and manufacturing, automated optical inspection (AOI), opto – mechatronics instrumentation and 3 – D machine vision and algorithms for automation. In publication, he has published one textbook, three book chapters, more than 100 referred journal papers and 60 invention patents internationally. For academic services, he served as the president of the international committee of measurement and instrumentation (ICMI) between 2015 – 2017 and currently serves as a steering committee member in ICMI and IMEKO. Meanwhile, he is also participating as a member in SPIE, SME, the Institution of Engineers of Australia (IEA) and Chinese Institute of Engineers (CIE), and a board member in Taiwan Society of Precision Engineering (TSPE), Automated Optical Inspection Equipment Association (AOIEA) and Chinese Metrology Society (CMS).